

A SEARCH FOR LEPTON FLAVOR VIOLATING DECAYS OF THE HIGGS BOSON
AND A MEASUREMENT OF W BOSON PRODUCTION USING THE CMS DETECTOR
AT THE LHC

by

Aaron Levine

A dissertation submitted in partial fulfillment of
the requirements for the degree of

Doctor of Philosophy

(Physics)

at the

UNIVERSITY OF WISCONSIN – MADISON

2016

Defended on

Dissertation approved by the following members of the Final Oral Committee:

Sridhara Dasu · Professor of Physics

Wesley Smith · Professor of Physics

Other Member · Professor of Physics

Other Member · Professor of Physics

Other Member · Professor of Other Department

Abstract

Abstract Goes Here

Acknowledgements

This is where any acknowledgements would go.

Contents

Abstract	i
Acknowledgements	ii
List of Tables	x
1 Theoretical Motivation	1
1.1 The Standard Model	1
1.1.1 Elementary Particles	2
1.1.2 Elementary Forces	3
1.1.3 The Higgs Boson	5
1.2 Beyond the Standard Model	6
2 Collider Phenomenology	8
2.1 Proton-Proton Collisions	8
2.2 W Boson Production: Mention prior results	10
2.3 Higgs Boson Production	11
3 Experimental Design: The Headings below are self explanatory	16
3.1 LHC	16
3.2 CMS	16
3.2.1 Overview	16
3.2.2 Tracker	16
3.2.3 ECAL	16
3.2.4 HCAL	16
3.2.5 Muon System	16

3.2.6	Trigger	16
4	Event Simulation	17
4.1	Monte Carlo Event Generation	17
4.1.1	Matrix Elements	18
4.1.2	Parton Showering	18
4.1.3	Hadronization	19
4.1.4	Monte Carlo Generator Software	19
4.2	Detector Simulation	20
5	Event Reconstruction	21
5.1	Particle Flow Overview	21
5.2	Electrons	23
5.3	Muons	24
5.4	Hadrons	24
5.4.1	Jets	25
5.4.2	Taus	26
5.5	Missing Energy	27
6	Analysis Methods: Summarize W+Jets and LFV Higgs ANs	28
6.1	Background Estimation	28
6.1.1	Monte Carlo Samples Used: This section will simply list the Monte Carlo samples used, in contrast with the Monte Carlo Generation section which will list the different Monte Carlo generator techniques.	28
6.1.2	QCD Estimation	29
6.1.3	Tau Embedding	29
6.1.4	Fake Rate Method	29
6.2	Selection Optimization	33
6.2.1	W+Jets	38
6.2.2	LFV Higgs	38
6.3	Systematic Uncertainties	38
6.3.1	W+Jets	38

6.3.2	LFV Higgs	38
7	Results	43
7.1	LFV Higgs	43
7.1.1	Statistical Methods	43
7.1.1.1	Maximum Likelihood Fit	43
7.1.1.2	Maximum Likelihood Limits	44
7.1.2	8 TeV Results	45
7.1.3	13 TeV Results	48
7.1.4	Limit computation	48
7.2	Limits on lepton flavour violating couplings	49
7.3	W+Jets	50
7.3.1	Detector Unfolding	50
7.3.2	13 TeV Results	51
8	Conclusions	52
8.1	Summary	52
8.2	Future Outlook	52
	Bibliography	53

List of Figures

1.1	The fundamental particles of the Standard Model. Charges are expressed in units of electron charge.[33]	3
1.2	Decay of the tau lepton, as mediated by the W boson. The W boson is discussed further in Section 1.1.2.	4
1.3	A photon mediating scattering between two electrons	4
1.4	The potential of the Higgs Field. Note the nonzero minima.	6
1.5	Loop contribution of lepton flavor violating couplings between muons and taus to the anomalous magnetic moment of the muon.	7
2.1	Diagram of jet formation occurring after a hard scatter event. First quarks and gluons are radiated in parton showering. Then they combine into colorless cluster before condensing into the hadrons that make up jets.	9
2.2	Diagram of W Boson production. The function F_1 and F_2 are the parton distribution functions of the incoming protons.	10
2.3	Parton distribution functions in the CTEQ6 scheme[34]. As the energy Q of the collision increases, the quarks involved carry less and less of the proton's momentum and the applicability of pQCD increases.	11
2.4	Example of the production of a W plus one jet event.	12
2.5	W+jets production at CMS in 2011. Cross sections are show in units of picobarns. The left plot shows exclusive jet binned ($= N_{\text{Jets}}$) results and the right plot shows inclusive jet binned ($\geq N_{\text{Jets}}$) results. Comparisons between theoretical predictions and data are shown in the ratio plots. Agreement is within statistical uncertainty.	13
2.6	Higgs production via gluon gluon fusion.	13
2.7	Higgs production via vector boson fusion.	14

2.8	Higgs production cross sections[20]. At a mass of 125 GeV, the two largest production modes are gluon gluon fusion and vector boson fusion.	14
2.9	Higgs decay branching ratios[7]. The mass of the Standard Model Higgs is 125 GeV.	15
4.1	An illustration of the Lund string model. As the quark/anti-quark pair move further apart, the increase in potential energy creates an additional quark/anti-quark pair.	19
5.1	A visual depiction of the iterative tracking algorithm. First, pixel triplets (in red) are identified. Secondly, the best match of pixel hits and track hits is identified. Finally, the identified track is removed and the algorithm finds the second best track candidate.	22
5.2	Performance of the anti- k_t algorithm. [13] Note that the anti- k_t algorithm is the only algorithm that generates a circular hard jet.	26
6.1	Left) $M_{collinear}$ for the $H \rightarrow \mu\tau_e$ same sign isolated e or μ plus isolated μ or e sample (region II). Right) $M_{collinear}$ for the $H \rightarrow \mu\tau_{had}$ same sign isolated muon plus tight-isolated tau (region II).	30
6.2	Distributions of M_{col} for region II compared to the estimate from scaling the region IV sample by the measured misidentification rates. The bottom panel in each plot shows the fractional difference between the observed data and the estimate. Left: $H \rightarrow \mu\tau_e$. Right: $H \rightarrow \mu\tau_{had}$	33
6.3	The collinear mass $M_{collinear}$ for signal ($B(H \rightarrow \mu\tau) = 100\%$ for clarity) and background after pre-selection requirements for the LFV $H \rightarrow \mu\tau$ decays for the different channels and categories compared to data. The shaded grey bands indicate the uncertainty. Top left: $H \rightarrow \mu\tau_e$ 0-jet , top right: $H \rightarrow \mu\tau_{had}$ 0-jet, middle left: $H \rightarrow \mu\tau_e$ 1-jet, middle right: $H \rightarrow \mu\tau_{had}$ 1-jet, bottom left: $H \rightarrow \mu\tau_e$ 2-jet, bottom right $H \rightarrow \mu\tau_{had}$ 2-jet.	35

6.4	Distributions of the collinear mass M_{col} for signal with $\mathcal{B}(H \rightarrow \mu\tau) = 100\%$ for clarity, and background processes after the loose selection requirements for the LFV $H \rightarrow \mu\tau$ candidates for the different channels and categories compared to data. The shaded grey bands indicate the total uncertainty. The bottom panel in each plot shows the fractional difference between the observed data and the total estimated background. Top left: $H \rightarrow \mu\tau_e$ 0-jet; top right: $H \rightarrow \mu\tau_h$ 0-jet; middle left: $H \rightarrow \mu\tau_e$ 1-jet; middle right: $H \rightarrow \mu\tau_h$ 1-jet; bottom left: $H \rightarrow \mu\tau_e$ 2-jet; bottom right $H \rightarrow \mu\tau_h$ 2-jet.	38
7.1	Distributions of the collinear mass M_{col} after fitting for signal and background for the LFV $H \rightarrow \mu\tau$ candidates in the different channels and categories compared to data. The distribution of the simulated LFV Higgs boson sample is shown for the best fit branching fraction of $\mathcal{B}(H \rightarrow \mu\tau) = 0.84\%$. The bottom panel in each plot shows the fractional difference between the observed data and the fitted background. Top left: $H \rightarrow \mu\tau_e$ 0-jet; top right: $H \rightarrow \mu\tau_h$ 0-jet; middle left: $H \rightarrow \mu\tau_e$ 1-jet; middle right: $H \rightarrow \mu\tau_h$ 1-jet; bottom left: $H \rightarrow \mu\tau_e$ 2-jet; bottom right $H \rightarrow \mu\tau_h$ 2-jet.	46
7.2	Left: 95% CL Upper limits by category for the LFV $H \rightarrow \mu\tau$ decays. Right: best fit branching fractions by category.	47
7.3	Distributions of the collinear mass M_{col} after fitting for signal and background for the LFV $H \rightarrow \mu\tau$ candidates in the different channels and categories compared to data. The distribution of the simulated LFV Higgs boson sample is shown for $\mathcal{B}(H \rightarrow \mu\tau) = 10\%$. The bottom panel in each plot shows the fractional difference between the observed data and the fitted background. Top left: $H \rightarrow \mu\tau_e$ 0-jet; top right: $H \rightarrow \mu\tau_h$ 0-jet; middle left: $H \rightarrow \mu\tau_e$ 1-jet; middle right: $H \rightarrow \mu\tau_h$ 1-jet; bottom left: $H \rightarrow \mu\tau_e$ 2-jet; bottom right $H \rightarrow \mu\tau_h$ 2-jet.	48
7.4	95% CL Upper limits by category for the LFV $H \rightarrow \mu\tau$ decays.	49

- 7.5 Constraints on the flavour violating Yukawa couplings, $|Y_{\mu\tau}|$ and $|Y_{\tau\mu}|$. The black dashed lines are contours of $\mathcal{B}(H \rightarrow \mu\tau)$ for reference. The expected limit (red solid line) with one sigma (green) and two sigma (yellow) bands, and observed limit (black solid line) are derived from the limit on $\mathcal{B}(H \rightarrow \mu\tau)$ from the present analysis. The shaded regions are derived constraints from null searches for $\tau \rightarrow 3\mu$ (dark green) and $\tau \rightarrow \mu\gamma$ (lighter green). The light blue region indicates the additional parameter space excluded by our result. The purple diagonal line is the theoretical naturalness limit $Y_{ij}Y_{ji} \leq m_i m_j / v^2$ 49

List of Tables

1.1 Fundamental forces of the Standard Model[25].	3
6.1 Schematic to illustrate the application of the method used to estimate the misidentified lepton background. Samples are defined by the charge of the two leptons and by the selection requirements on each. The selection requirement and charge requirement is altered on the second lepton to define four regions.	30
6.2 Definition of the samples used to estimate the misidentified lepton (ℓ) background. They are defined by the charge of the two leptons and by the isolation requirements on each. . .	32
6.3 Selection criteria requirements for the kinematic variables after pre-selection.	34
6.4 Selection criteria for the kinematic variables after the loose selection.	36
6.5 Signal region definition	37
6.6 Systematics. All systematics are treated as correlated between the categories, except where there are two numbers. In this case the number denoted with * is treated as uncorrelated between categories.	39
6.7 Systematic uncertainties in the expected event yield in %. All uncertainties are treated as correlated between the categories, except where there are two numbers. In this case the number denoted with * is treated as uncorrelated between categories and the total uncertainty is the sum in quadrature of the two numbers.	39
6.8 Theoretical Uncertainties in Higgs production.	40
6.9 Theoretical uncertainties in % for Higgs boson production. Anticorrelations arise due to migration of events between the categories and are expressed as negative numbers. . . .	40
6.10 Systematic uncertainties in % for the shape of the signal and background templates. . . .	40
6.11 Systematic uncertainties in the shape of the signal and background templates.	40

6.1	Systematic uncertainties in the expected event yield in %. All uncertainties are treated as correlated between the categories, except where there are two values. In this case the first value is correlated as above, while the second value (following \oplus) represents an uncorrelated uncertainty for each individual category. The total uncertainty in a given category is the sum in quadrature of the two values.	42
7.1	Event yields in the signal region, $100 < M_{\text{col}} < 150\text{GeV}$ after fitting for signal and background. The expected contributions are normalized to an integrated luminosity of 19.7 fb^{-1} . The LFV Higgs boson signal is the expected yield for $B(H \rightarrow \mu\tau) = 0.84\%$ with the SM Higgs boson cross section.	45
7.2	The expected upper limits, observed upper limits and best fit values for the branching fractions for different jet categories for the $H \rightarrow \mu\tau$ process. The one standard-deviation probability intervals around the expected limits are shown in parentheses.	47
7.3	Event yields in the signal region in the range $100 < M_{\text{col}} < 150\text{GeV}$. The expected contributions are normalized to an integrated luminosity of 2.3 fb^{-1} . The LFV Higgs boson signal is the expected yield for $B(H \rightarrow \mu\tau) = 1\%$ with the SM Higgs boson cross section.	48
7.4	The observed and expected upper limits for different jet categories for the $H \rightarrow \mu\tau$ process. The one standard deviation probability intervals around the expected limits are shown in parentheses.	49

Chapter 1

Theoretical Motivation

In high energy particle physics, the goal is to use high energy densities to probe small distance scales and investigate properties of fundamental particles and the forces that govern them. This thesis describes the search for an exotic, lepton flavor violating, interaction between a Higgs boson, a muon, and a tau. These concepts are defined in subsequent sections of this chapter. This interaction has never been observed in nature and is prohibited by the Standard Model, the most comprehensive theory of particle interactions to date. If observed, these lepton flavor violating couplings would represent signs of a deeper theory that would significantly enhance our perception of forces and particles. This thesis also contains the measurement of W boson production and associated jets. This process involves key forces and particles of the Standard Model, and precise measurements of the process will improve understanding of the existing theory. These measurements take place at the Compact Muon Solenoid (CMS) detector using the Large Hadron Collider (LHC).

1.1 The Standard Model

Our knowledge of particle interactions is summarized in a theory called the Standard Model. The theoretical framework of the Standard Model was developed over the course of the 20th century as more and more fundamental particles and forces were discovered and studied. The Standard Model is not without its flaws. It is a phenomenological theory that contains many free parameters, such as the masses of the particles, that can only be determined from experiment. It also fails to include the gravitational interactions, and thus only describes three of the four fundamental forces. The ad hoc design of the Standard Model and the lack of unification provides a strong motivation

for particle physicists to search for a more profound, comprehensive theory. The current state of particles physics takes a two pronged approach, with physicists making precision measurements of the Standard Model and searching for physics beyond the Standard Model. The goal is to measure the parameters of the Standard Model while searching for the theory's extension. This thesis contains both aspects. The W+jets production cross section measurement directly tests the Standard Model while the search for lepton flavor violating Higgs couplings tests hypotheses that extend the theory.

1.1.1 Elementary Particles

The fundamental particles in the Standard Model are summarized in Figure 1.1. The fundamental particles consist of fermions and bosons. The fermions are particles that have half integer spin, and the bosons have integer spin. Spin is the intrinsic quantized angular momentum of a particle. The bosons mediate the fundamental forces and provide mass. They will be discussed further in Section 1.1.2 and Section 1.1.3. The fermions consist of the quarks, leptons, and neutrinos.

There are three generations of quarks, with two flavors in each generation. Each quark generation consists of a quark with $+2/3$ of an electron charge ($+2/3e$) and a quark with $-1/3$ of an electron charge ($-1/3e$). Quarks also have a property known as "color." There are three possible colors for each quark: red, green, or blue. The concept of color is important for understanding the strong nuclear force, as discussed in Section 1.1.2. As shown in figure 1.1 the masses of the quarks vary significantly from one generation to the next.

Free quarks have never been observed in nature. Only color neutral combinations of quarks have been observed. For example, a red, green, or blue quark can form a stable state with a corresponding antiquark, with an anticolor of antired, antigreen, or antiblue. This state is known as a meson. The baryons consists of three quarks, one of each color. The proton (uud), and the neutron (udd), are both baryons. Matter than is composed of quarks is called hadronic matter. At CMS, hadrons are often found in collimated streams of particles known as jets.

There are three generations of leptons, each with a neutrino pair. The electron is extremely light and does not decay, but the muon and the tau are heavier and have lifetimes on the order of $10^{-6}s$ and $10^{-15}s$ respectively[33]. The mechanisms for lepton decay will be discussed in Section 1.1.2 . In the Standard Model, there is a conserved quantity known as the lepton number. Each lepton/neutrino pair, such as an e and an ν_e each will have an electron lepton number of 1, and the corresponding antiparticle pair will have a lepton number of -1. Figure 1.2 gives an example of

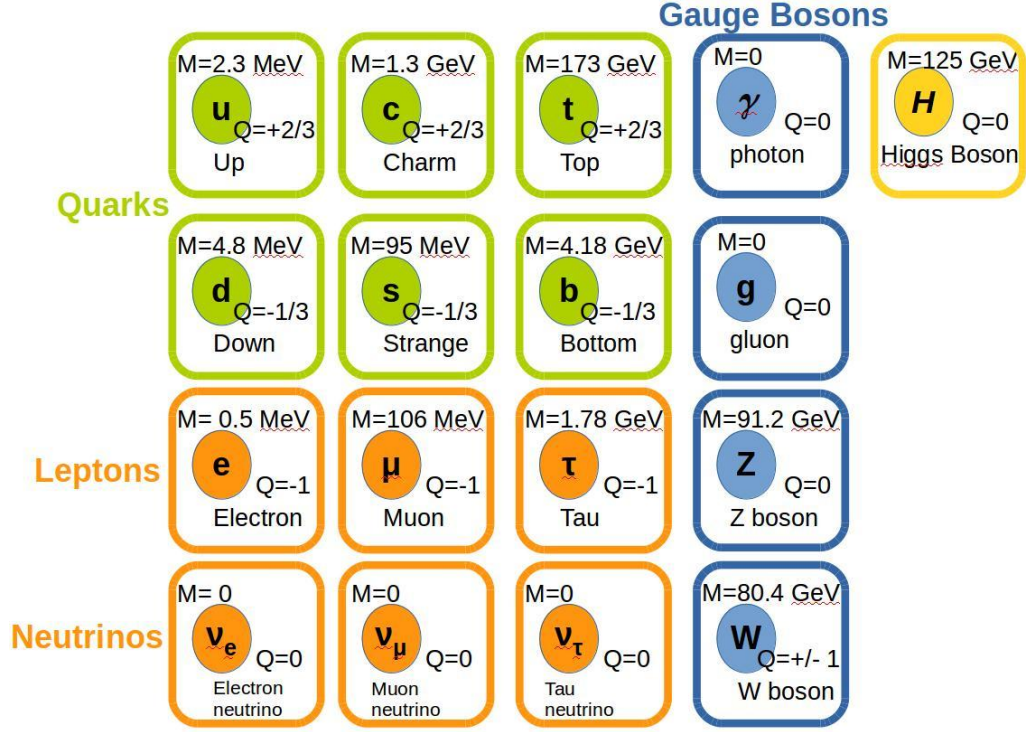


Figure 1.1: The fundamental particles of the Standard Model. Charges are expressed in units of electron charge.[33]

a decay that conserves lepton number. In the initial state only the tau exists and the tau lepton number of the system is one while the muon and electron lepton numbers of the system are 0. The decay produces a tau neutrino which also has a tau lepton number of one along with an electron and an antielectron neutrino, which have electron lepton numbers of one and negative one, respectively. So the final state also has a tau lepton number of one. Also note that lepton number and flavor are conserved at each vertex. In the lepton flavor violating couplings studied in this thesis, a muon and a tau share a vertex, which is not allowed in the standard model.

1.1.2 Elementary Forces

Force	Relative Strength	Mediator
Strong	1	Gluon
Electromagnetic	10^{-3}	Photon
Weak	10^{-11}	W,Z Boson

Table 1.1: Fundamental forces of the Standard Model[25].

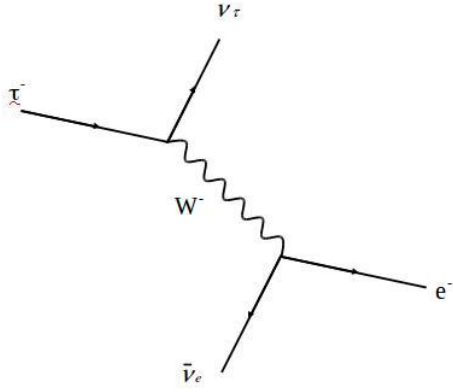


Figure 1.2: Decay of the tau lepton, as mediated by the W boson. The W boson is discussed further in Section 1.1.2.

The fundamental forces of the Standard Model are shown in Table 1.1. Note that gravity is not included in the table. Gravity is not contained in the standard model and has a strength on the order of 10^{-30} [9] relative to the weak nuclear force. It plays a negligible role in high energy physics.

The theory of the electromagnetic is known as quantum electrodynamics (QED). The electromagnetic force is mediated by the photon. The photon is a spin 0 massless particle. Two examples of electromagnetic interactions are shown in figure 1.3. This figure displays an example of a Feynman diagram, which are pictorial representations of particle interactions that are also used to calculate the matrix elements and amplitudes of the process. Matrix elements are used to compute the cross sections, which, as described in chapter 2, are a measurement of the likelihood of the process occurring. The photon only interacts with particles that carry charge.

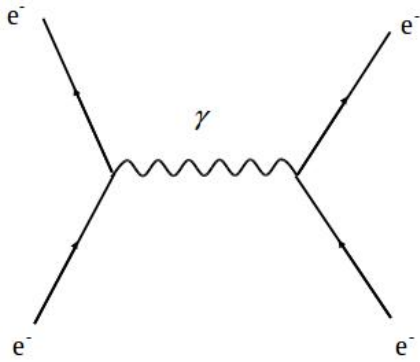


Figure 1.3: A photon mediating scattering between two electrons

The weak nuclear force is mediated by the W and Z bosons. The Z boson is a neutral spin 1 particle. It decays into pairs of quarks, leptons, or neutrinos. The W boson is a charged spin 1 particle. It has the special property of changing flavors of quarks and leptons. For example, the W boson can mediate the decay of a tau to an electron. This is illustrated in figure 1.2. Note that lepton number is still conserved in these types of interactions.

The theory of the strong nuclear force is known as quantum chromodynamics (QCD). The strong nuclear force is mediated by the gluon. Each gluon is a color doublet, with a corresponding color and anticolor. For example, a gluon could be red and antired, or blue and antiblue, et cetera. Gluons only interact with particles that share one of their color charges. Therefore, the quarks are the only particles involved in strong interactions. Virtual gluons can self interact which increases the strength of the color charge surrounding a quark. At small distance scales the virtual gluon cloud is penetrated and the effective color charge decreases. This effect is known as asymptotic freedom. [25] At larger distances, as a quark antiquark pair move apart from each other, the increase in potential energy allows new quark antiquark pairs to be created from the vacuum. The new quarks will be bound to the initial quarks by the strong nuclear force, which is why free quarks have never been observed. The coupling constant for QCD, α_s , is energy dependent and scales as $\alpha_s(Q^2) \propto 1/\ln(\frac{Q^2}{\Lambda_{QCD}^2})$. Here Q^2 represents the momentum transfer of the process and Λ_{QCD} is a constant, referred to as the QCD scale, with a measured value of 214 MeV[33]. At the TeV scale collision energies of the Large Hadron Collider, α_s is small and interactions are modelled using perturbative QCD (pQCD). Leading order terms that depend on α_s and next to leading order terms that depend on α_s^2 dominant the computation and higher order terms can be neglected.

As mentioned in chapter 2.2 both the strong force and the weak force play important roles in the production of W bosons and associated jets. The strong force governs quark-gluon interactions and jet formation, while the weak force is responsible for the W boson couplings to initial state quarks and final state leptons. Thus, a precision measurement of W+jets production is a powerful channel to evaluate the accuracy of the Standard Model.

1.1.3 The Higgs Boson

In classical physics, the equations of motion of a system are governed by the Lagrangian. The Lagrangian is defined as $L = T - V$ where T is the kinetic energy and V is the potential energy. In the Standard Model, we can also define a Lagrangian that governs all particle interactions[25]

However, when mass terms for W and Z bosons are added to the Lagrangian, the Standard Model breaks down. Loops formed by W and Z bosons contribute infinities to Standard Model calculations that cannot be removed. This means that the Standard Model becomes unrenormalizable.

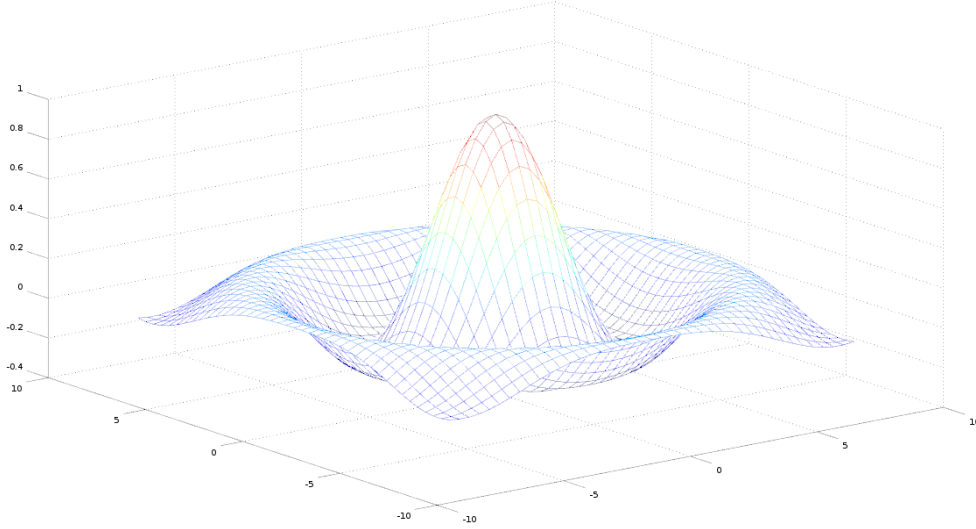


Figure 1.4: The potential of the Higgs Field. Note the nonzero minima.

To resolve this, we introduce a field with a potential shown in figure 1.4. This potential has a minimum that is not at the origin of the coordinate system. We can break the symmetry by shifting our reference point to the minimum of the potential and expanding for small deviations about the minimum. When this shift is introduced to the Lagrangian, it results in mass terms appearing for the W and Z bosons, the quarks and leptons, and a mass term for the particle associated with the field itself. That particle is known as the Higgs Boson. In addition to providing the theoretical framework to add mass terms to the Lagrangian, the Higgs Boson couples to every massive particle in the Standard Model. The couplings of the Higgs to the W and Z bosons cancel out the infinities mentioned earlier.[25] Thus, the field that naturally gives rise to masses in the Standard Model also cancels out the divergences that prevented us from simply placing mass terms in the Lagrangian to begin with. A Higgs Boson with a mass of 125 GeV was discovered at CERN on July 4 2012. [33]

1.2 Beyond the Standard Model

As mentioned in Chapter 1 Standard Model requires many free parameters determined by experiment and fails to unify gravity with the other four fundamental forces. Additionally, it fails to

account for neutrino oscillations[23][2][3] and it doesn't address the hierarchy problem. [8] A more fundamental theory must exist, and the recently discovered Higgs boson provides a rich environment for probing the existence of such a theory. Many proposed theories such as Randall-Sundrum models [35] or Two Higgs Doublet models [12] predict a Higgs boson with couplings that violate lepton flavor conservation. The strength of Higgs couplings are proportional to the masses of the particles involved, so the most logical place to start a search for lepton flavor violation would be a Higgs boson coupling directly to the two heaviest leptons: a muon and a tau.

There have been no direct searches for $H \rightarrow \mu\tau$ prior to the result contained in this dissertation. Null searches for $\tau \rightarrow \mu\gamma$ constrain the branching fraction for $H \rightarrow \mu\tau$ to $\mathcal{O}(10\%)$. [26]

Lepton flavor violating couplings may explain a discrepancy in the anomalous magnetic moment of the muon. The magnetic moment is a quantity defined for a current loop that describes the torque the current loop experiences in a magnetic field. Muons are point particles, so according to classical electrodynamics they lack a magnetic moment. However, in QED, loop interactions will effectively generate a magnetic moment, known as the anomalous magnetic moment of the muon. The current measured value differs from the expected standard model value by 2.87×10^{-9} , a significance of 3.6σ [10][33]. Loop corrections, as shown in Figure 1.5 from a Higgs coupling to a muon and a tau could resolve this discrepancy [26].

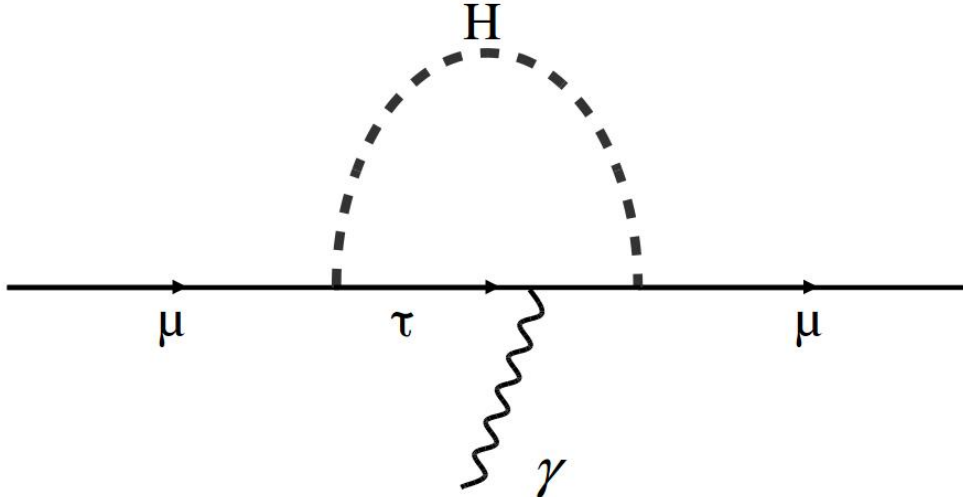


Figure 1.5: Loop contribution of lepton flavor violating couplings between muons and taus to the anomalous magnetic moment of the muon.

Chapter 2

Collider Phenomenology

Now that the underlying physics has been described in Chapter 1, the question remains: how exactly are W+Jets and lepton flavor violating Higgs events produced and studied? Before proceeding further, it is necessary to define some basic terms of collider physics. The cross section of a particle interaction is an effective area that gives a sense of the likelihood of the interaction. In collider physics, cross sections are measured in barns (b), where $1b = 10^{-24}cm^2$. The luminosity is defined as the rate of observed events divided by the cross section. The integrated luminosity is computed by integrating the luminosity with respect to time. Integrated luminosity is used to define how much total data a collider has supplied. These terms will be used for describing proton proton collisions, W boson production, and Higgs boson production in the coming sections of this chapter.

2.1 Proton-Proton Collisions

The Large Hadron Collider (LHC), which will be discussed further in Chapter 3, is a proton-proton collider. The proton, as mentioned in Chapter 1, is considered to be the bound state of three quarks: two up quarks and a down quark. However, proton-proton collisions cannot simply be thought of as six up and down quarks interacting. Inside the proton, massive amounts of quark and antiquark pairs pop in and out of existence. At the high energies and short distance scales probed by the LHC, these "sea quarks" play a dominant role in proton proton collisions. The gluons that bind elements of the quark/antiquark sea also play a large role in collisions. In fact, these gluons carry about 50% of the proton's momentum[25]. So when two protons collide at the LHC, it is effectively a collision between two clouds of gluons and quarks. These collisions can be studied via

the parton model. This model defines the protons as collections of point particles (partons) carrying a fraction x of the hadron's momentum. The distribution of x depends on the momentum scale Q^2 that is probed.

When these clouds of gluons and quarks collide, most of the collisions involve a small amount of momentum transfer between the particles involved. These are known as "soft" scattering. The important processes, such as W boson or Higgs boson production, require a "hard" scattering event. These types of events seldom happen more than once each time the clouds of gluons and quarks intersect. Therefore, for each interesting hard scattering event there will be many soft scattering events occurring at the same time. The soft scattering events are referred to as pileup.

As quarks and gluons move apart after the collision, the increase in potential energy from the strong interaction produces a stream of collimated hadrons, known as a jet. Jet formation is shown in Figure 2.1. First, energetic quarks radiate gluons, which split into quarks. These quarks may still be energetic enough to radiate gluons, and the process continues. This is known as parton showering. Detailed simulations are described in chapter 4. After the conclusion of parton showering, hadronization occurs. QCD confinement requires that the quarks and gluons are naturally grouped into colorless clusters. These clusters then separate into groups of hadrons, which is known as hadronization. The identification of jets is discussed in Chapter 5.

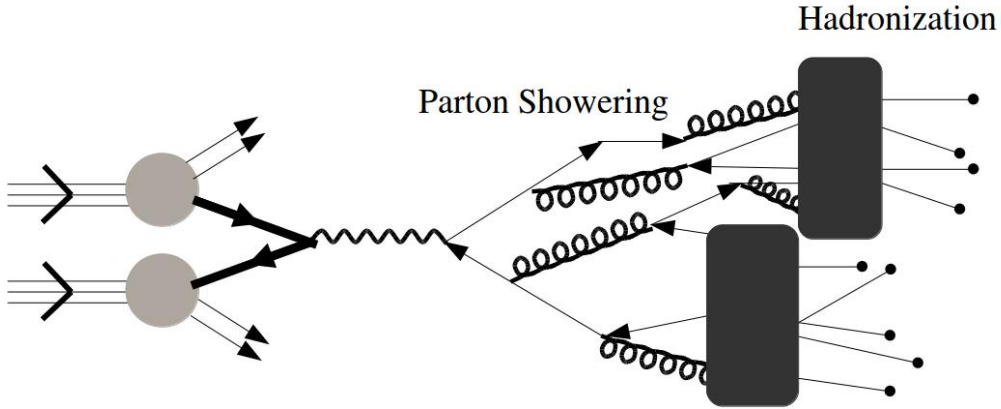


Figure 2.1: Diagram of jet formation occurring after a hard scatter event. First quarks and gluons are radiated in parton showering. Then they combine into colorless cluster before condensing into the hadrons that make up jets.

2.2 W Boson Production: Mention prior results

W bosons are produced by deep inelastic scattering between partons, as show in Figure 2.2. The cross section of this process depends on the parton distribution functions. Examples of CTEQ6 parton distribution functions are show in Figure ??[34]. These parton distribution functions are used in PYTHIA (chapter 4).

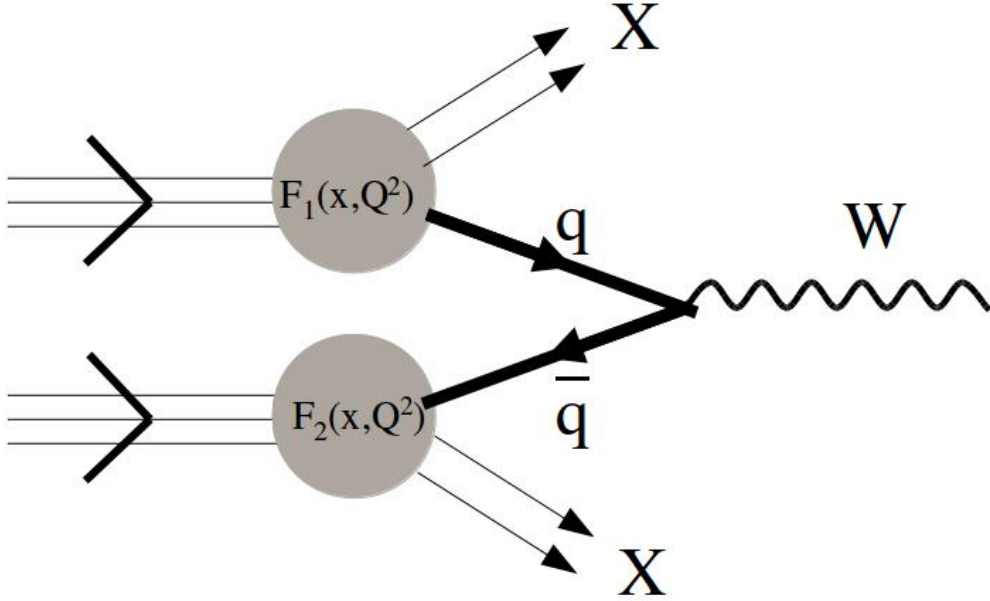


Figure 2.2: Diagram of W Boson production. The function F_1 and F_2 are the parton distribution functions of the incoming protons.

W bosons decay to leptons and quarks at equal rates. The W may decay to an up/down quark pair, a charm/strange quark pair, or a lepton/lepton neutrino pair. The presence of the muon neutrino in the final state is necessary to conserve lepton flavor in the standard model, as discussed in Chapter 1. The decay to a bottom/top quark pair is suppressed because of the high mass of the top quark. Each quark has three flavors, and there are three total leptons, so ultimately W decay has six hadronic final states and three leptonic final states. This means that W bosons decay to hadrons approximately 67% of the time and decay to leptons about 33% of the time. As discussed in Chapter 3 and Chapter 5, due to CMS's ability to reconstruct muons, we look for W bosons decaying to a muon and a muon neutrino. Because of lepton universality, the branching fraction of $W \rightarrow \mu\nu_\mu$ is about 11%.

W boson production is studied based on the number of jets produced in association with the

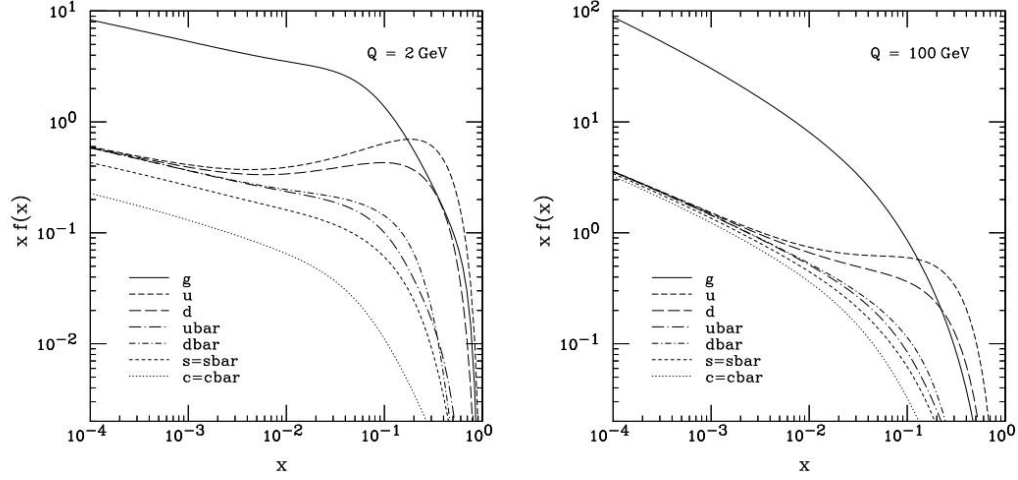


Figure 2.3: Parton distribution functions in the CTEQ6 scheme[34]. As the energy Q of the collision increases, the quarks involved carry less and less of the proton's momentum and the applicability of pQCD increases.

W boson. An example of a single radiated jet is show in Figure 2.4. The cross section for W boson from two partons scattering is given by equation 2.1 [9]. Here, V_{ud} is a matrix element that defines the probability for up-down quark transition, G_F is a fundamental constant, M_W is the mass of the W boson, and \hat{s} is the momentum of the diquark system. The hats on \hat{s} and $\hat{\sigma}$ indicate that these values apply to one parton scattering off of another parton. To calculate the full cross section of W production we must integrate over the parton distribution functions of the quarks involved.

$$\hat{\sigma}(ud \rightarrow W) = 2\pi|V_{ud}|^2 \frac{G_F}{\sqrt{2}} M_W^2 \delta(\hat{s} - M_W^2) \quad (2.1)$$

Previous results from CMS measured at 7 TeV center of mass collisions[28] are show in Figure 2.5.

2.3 Higgs Boson Production

As discussed in Chapter 1, Higgs boson couplings are mass dependent. The more massive the particle, the more likely it will couple to the Higgs. Top quarks, with a mass of 172 GeV, are the heaviest standard model particle. As a result, the dominant method of Higgs production is when two energetic gluons fuse together via create a top quark loop, as shown in Figure 2.6. This is called gluon-gluon fusion.

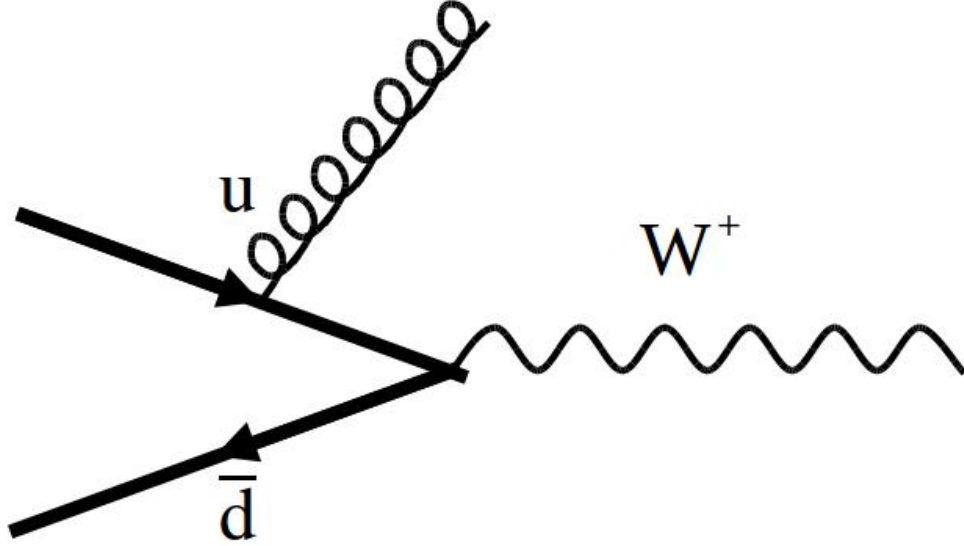


Figure 2.4: Example of the production of a W plus one jet event.

Vector boson fusion is the dominant mechanism of two jet Higgs boson production. It is shown in Figure 2.7. Because of conservation of color, the two final state quarks must be the same color as their corresponding initial state quarks. This will force the jets produced by the final state quarks apart at a wide angle. A graphic of all the Higgs production channels is shown in Figure 2.8[20].

There is no known Higgs branching ratio to guide this search. This is the first direct measurement of $H \rightarrow \mu\tau$. The kinematics of this search are similar to the kinematics $H \rightarrow \tau\tau$ search carried out at CMS [14]. As discussed in chapter 5.4.2, tau leptons are detected at CMS via their hadronic decay mode (τ_h) or their leptonic decay modes (τ_e, τ_μ). Therefore, the final state objects, a muon and a tau, are exactly the same between $H \rightarrow \mu\tau$ and the $H \rightarrow \tau_{\mu u}\tau$ channel of $H \rightarrow \tau\tau$, making $H \rightarrow \tau\tau$ a major background of the search. A major difference between $H \rightarrow \tau_{\mu u}\tau$ and $H \rightarrow \mu\tau$ is the distribution of missing transverse energy (MET) in the event. MET, which is discussed further in chapter 5.5, arises from neutrinos that CMS cannot detect. As shown in figure 1.2, neutrinos are always associated with tau decays. The $H \rightarrow \tau_{\mu u}\tau$ channel will contain a muon neutrino associated with the muonic decay of the tau, but $H \rightarrow \mu\tau$ contains no such neutrino. The only neutrinos will be associated with the tau decay. The MET distribution will be used to define the signal region in chapter 6. A graphic of Higgs boson decay probabilities is shown in Figure 2.9[7]

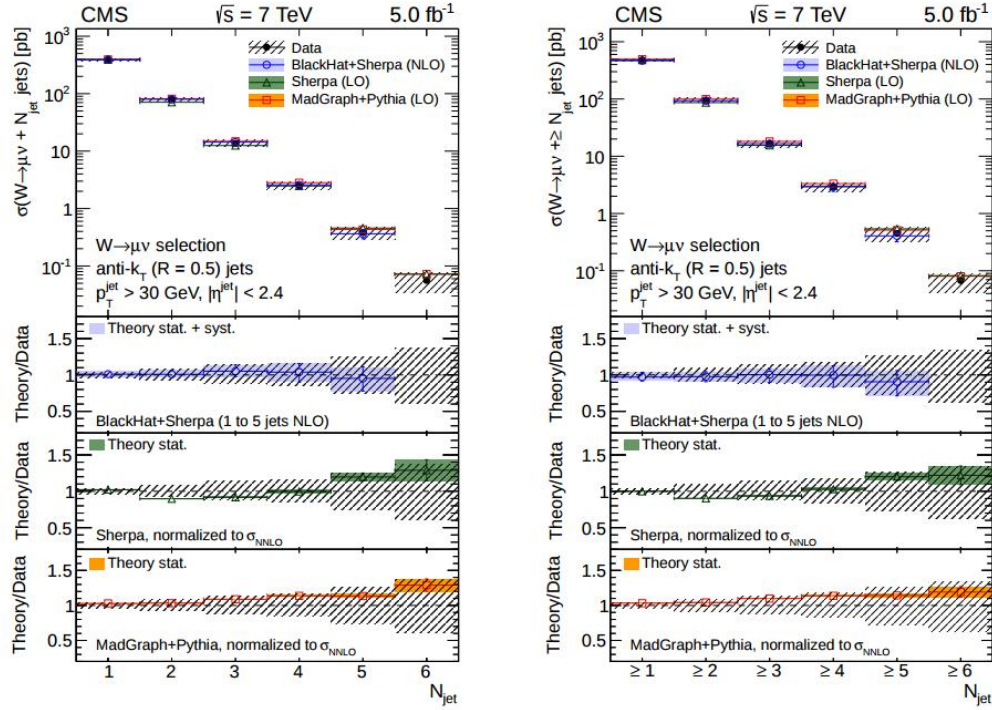


Figure 2.5: W +jets production at CMS in 2011. Cross sections are shown in units of picobarns. The left plot shows exclusive jet binned ($= N_{\text{Jets}}$) results and the right plot shows inclusive jet binned ($\geq N_{\text{Jets}}$) results. Comparisons between theoretical predictions and data are shown in the ratio plots. Agreement is within statistical uncertainty.

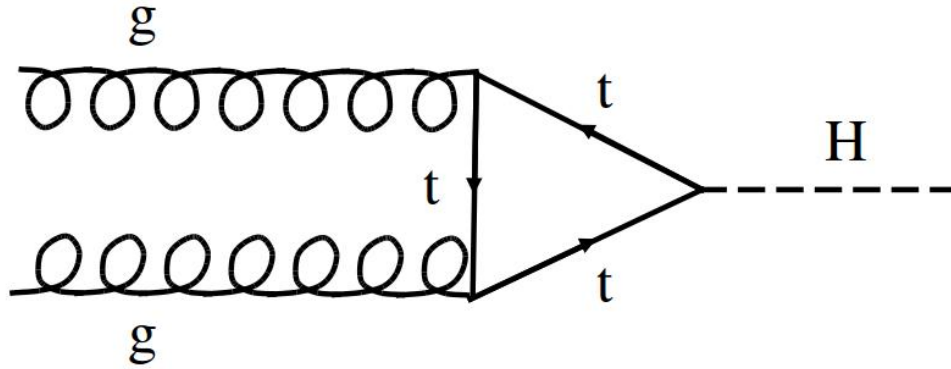


Figure 2.6: Higgs production via gluon fusion.

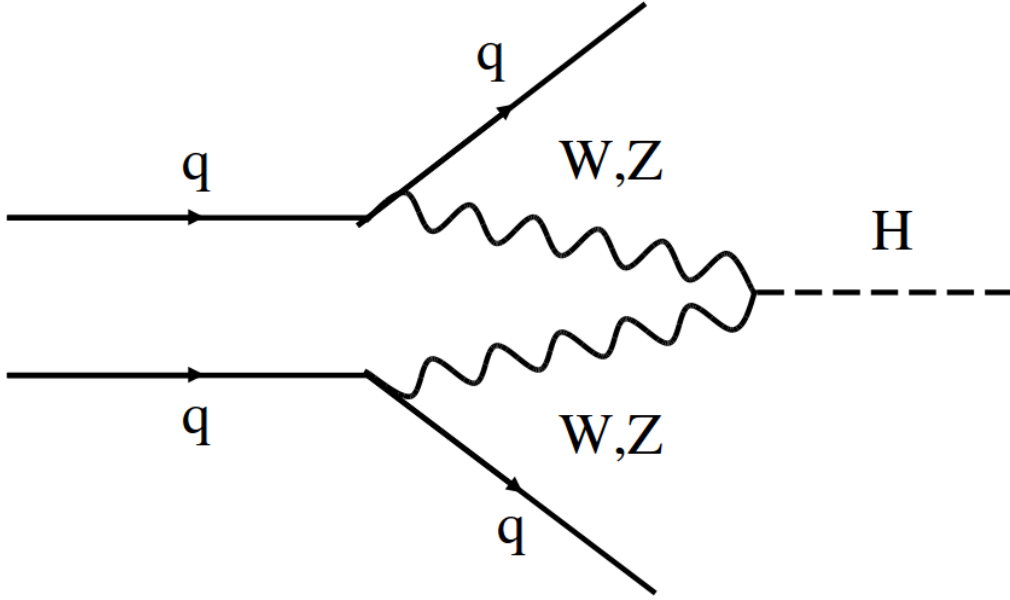


Figure 2.7: Higgs production via vector boson fusion.

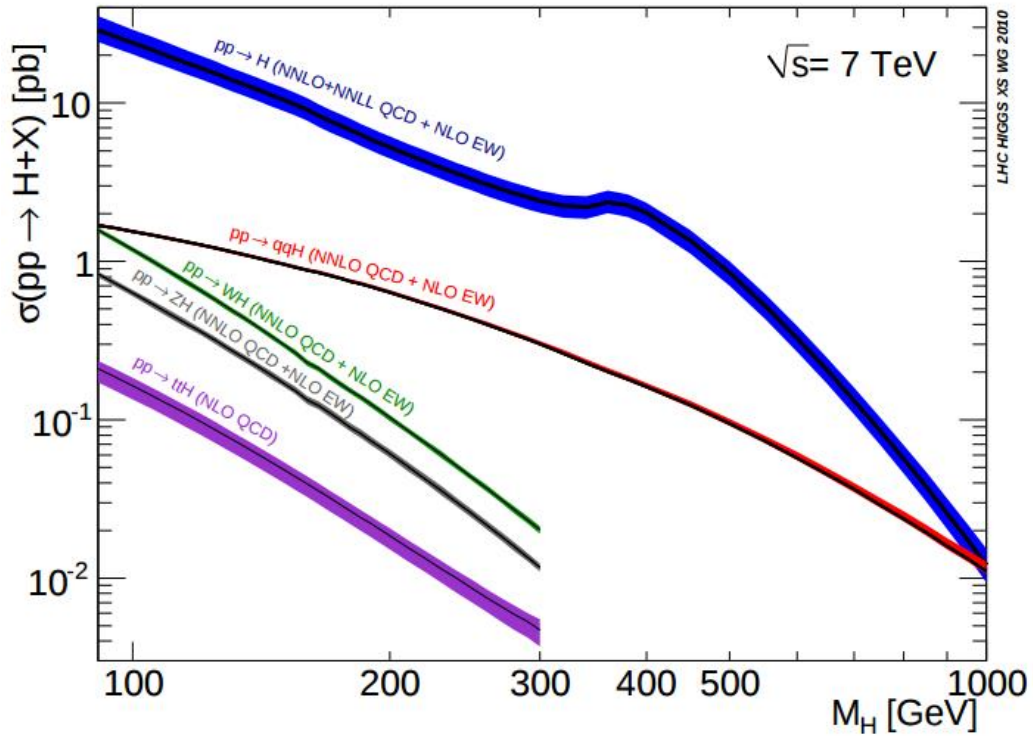


Figure 2.8: Higgs production cross sections[20]. At a mass of 125 GeV, the two largest production modes are gluon gluon fusion and vector boson fusion.

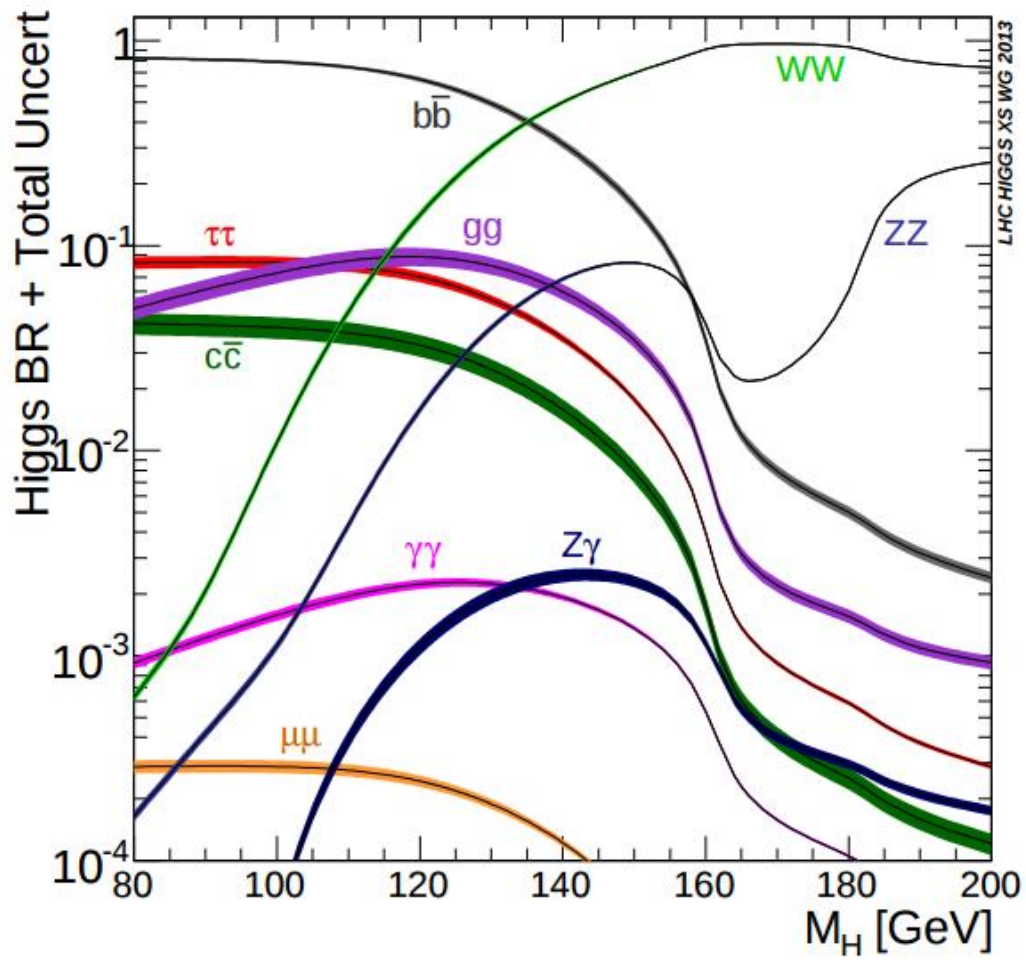


Figure 2.9: Higgs decay branching ratios[7]. The mass of the Standard Model Higgs is 125 GeV.

Chapter 3

**Experimental Design: The Headings
below are self explanatory**

3.1 LHC

3.2 CMS

3.2.1 Overview

3.2.2 Tracker

3.2.3 ECAL

3.2.4 HCAL

3.2.5 Muon System

3.2.6 Trigger

Chapter 4

Event Simulation

Particle interactions at CMS are computationally intensive to model. The strong nuclear force plays a dominant role in proton-antiproton collisions, but calculations involving QCD depend on large numbers of terms that define interactions between many quarks and gluons. At short distances, on the order of a femtometer, we can define the momentum scale Q to be much greater than Λ_{QCD} , as defined in chapter ?? This means that the effects of QCD can be calculated perturbatively (pQCD), which means that high order terms can be neglected and the calculations can be simplified. However, there are large amounts of soft radiation at Λ_{QCD} , as explained in chapter 2.1, which necessitates the use of computational software. The interactions of the collision products with the the detector also need to be modelled via simulation. Accurate models of physical processes at CMS are vital for testing existing theories and searching for new ones, so accurate modelling of these processes is very important for CMS and for particle physics in general.

4.1 Monte Carlo Event Generation

Physical processes at CMS are simulated using a class of software called Monte Carlo generators. These programs are named after the location of the famous casino because Monte Carlo software leans heavily on random number generation to simulate the kinematic distribution and decay chains of the event products. When using Monte Carlo software to simulate collisions, the user must specify the center of mass energy, the initial colliding particles, and the desired final products. Additional parameters can be defined by the user, such as the hadronization scale discussed in chapter 4.1.3. The three main components of Monte Carlo simulation are matrix element computation, parton

showering, and hadronization.

4.1.1 Matrix Elements

Once the initial and final state particles are specified, a series of Feynman diagrams are created. From the matrix elements discussed in chapter 1, production amplitudes are computed for the process. However, this calculation provides only a very basic picture of the event and neglects soft radiation at the pQCD scale.

4.1.2 Parton Showering

As discussed in chapter 2, in high energy collisions protons can be modeled as collections of partons where the partons are pointlike particles carrying a particular fraction of the proton's momentum. Parton distribution functions, as discussed in chapter 2, provide a model of how the protons will interact in a collision.

After the proton-proton collisions, Sudakov Form Factors[33] are computed, which represent the probability of a parton splitting into multiple partons. A low momentum bound for splitting is defined, and all partons above this threshold are randomly split in accordance with the probability of splitting. Color is properly accounted for at each vertex. Parton showers simulate QCD radiation emitted by quarks in the form of gluons, or a gluon splitting into two quarks.

At this point it is necessary to reconcile the matrix element computation, which represents high energy hard scattering, with parton showers, which model soft radiation. Two methods are available. The matrix element and parton shower method (ME+PS) and the next to leading order and parton shower method (NLO+PS)[33]. In the ME+PS method, matrix elements are computed for the fundamental process with the addition of n partons. The additional partons are required to be separated by a specified transverse momentum threshold. The momentum threshold is chosen to be at the upper limit of pQCD. In this way, the event can be computed accurately at large angle via matrix element methods, and then parton showering algorithms can be applied to the additional partons in the event. The ME+PS method is good for simulating events with many hard jets that are well separated. These kind of jets are simulated much better with tree level computations rather than lower energy pQCD parton showering. The next to leading order and parton shower method (NLO+PS) extends to parton shower method to next to leading order to QCD.

4.1.3 Hadronization

After parton showering, the event consists of the hard final products and many soft partons, as defined in chapter 2.1. At this point, the partons must transform into color singlet final state hadrons. One way to do this is the Lund string model[?]. In this model, quark and anti-quark pairs are connected by color "strings" with a potential $V(r) = \kappa r$, where r refers to the distance between the quarks and κ is a dimensionless constant that defines the strength of the potential. Since the potential is directly proportional to the distance between the quark pairs, the energy of the system increases as the quarks move further apart. Eventually, the energy of the system is enough to generate an additional quark/anti-quark pair, which effectively breaks the string into two separate strings, as shown in figure 4.1. The p_T of the quark or anti-quark is $\langle p_T^2 \rangle = \kappa/\pi$ and the Lund fragmentation function[33] defines the fraction of the longitudinal momentum of the endpoint particle that is imparted to its recently produced neighbor. In this fashion, the kinematic variables of the produced hadrons are known, and the shower continues until an energy scale cutoff is reached.

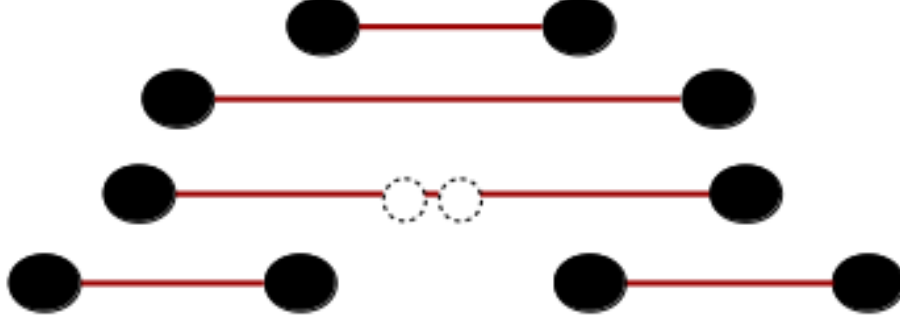


Figure 4.1: An illustration of the Lund string model. As the quark/anti-quark pair move further apart, the increase in potential energy creates an additional quark/anti-quark pair.

4.1.4 Monte Carlo Generator Software

A variety of different Monte Carlo generators are used at CMS. MADGRAPH [6] is used to compute matrix elements. Next to leading order (NLO) matrix elements can be computed with the aMC@NLO[6] version of MADGRAPH or with POWHEG[4, 21, 32]. NLO calculations are vital for accurately depicting physical processes such as W+Jets or Z+Jets. These calculations include quark and gluon loops that complement the fundamental hard scattering process. However, MAD-

GRAPH and POWHEG do not include parton showering and hadronization, which are necessary for accurate modelling of proton-proton collisions and jet formation, as discussed in chapter 2.1. The output of the matrix element generators are piped into PYTHIA, which models parton showers and hadronization using the Lund String Model. While PYTHIA is a powerful tool for calculating parton showering and hadronization, it is only a leading order (LO) generator, so it must receive matrix element results MADGRAPH or POWHEG to give results at the desired degree of precision. After hadronization, some heavy states may still need to decay. The τ lepton is too short lived to be directly observed in the detector, so any Monte Carlo simulation must decay the τ further. TAUOLA [38] is interfaced with PYTHIA to provide an accurate view of τ decay by taking into account τ helicity and polarization.

4.2 Detector Simulation

After the simulation of the physical process, complete with parton showering and hadronization, it is necessary to model the interactions of the finale state particles with the CMS detector. This is done using GEANT4[5]. First, an accurate model of the CMS detector must be built in GEANT4, defining both the geometry and material components of the detector. The simulation is then carried out in two steps: tracking and detector response. The tracking step simulates the passage of particles through matter, modelling the energy lost based on the particles and the detector material. The next step is to model the detector response. This will simulate the signal that each event will create. After the the GEANT4 simulation has completed, the output is converted to the same software format as the actual data and then reconstructed with the same algorithms discussed in chapter 5. The fully simulated events will retain all of the original Monte Carlo scattering information, so we can now understand what a particular physical process will look like from the point of view of the CMS detector. This allows us to study and improve the reconstruction of data, as discussed in chapter 5.

Chapter 5

Event Reconstruction

Studying physical processes requires reconstructing the particles in each event from the detector response. This is accomplished via the particle flow algorithm, which is discussed in Section 5.1. Specific applications to physics objects are discussed in subsequent sections of this chapter. In particular, the important objects for $H \rightarrow \mu\tau$ are muons, electrons, hadronic tau deposits, jets, and missing energy. The important objects for W+Jets are muons, jets, and missing energy.

5.1 Particle Flow Overview

As discussed in Section 3.2, the CMS detector is divided into many layers, each of which is responsible for measuring a unique part of an event. The detector response from each layer can be thought of as a building block for an event. Particle flow uses a series of algorithms to link these blocks to reconstruct the particles in the event. More specifically, particle flow algorithms link tracks in the tracker to energy deposits in the calorimeters or tracks in the muon system. Energy deposits that have no tracks associated with them are due to neutral particles. Ultimately, effective tracking algorithms are necessary before most particles can be identified.

Tracking algorithms build up the full tracks iteratively. Track construction begins by identifying hits in the pixel layer. There must be hits in at least three pixel layers with an energy of at least 200 MeV [16] These collections of hits are used to seed a track. The track is then propagated to subsequent layers of the tracker by a Kalman Filter technique [22]. A χ^2 fit is then used to identify the silicon strip hits that best correspond to the pixel triplets. All hits in the track are then

removed from the list of hits to consider, and the algorithm is repeated for subsequent collections of pixel triplets and silicon strip deposits. This is shown in figure 5.1.

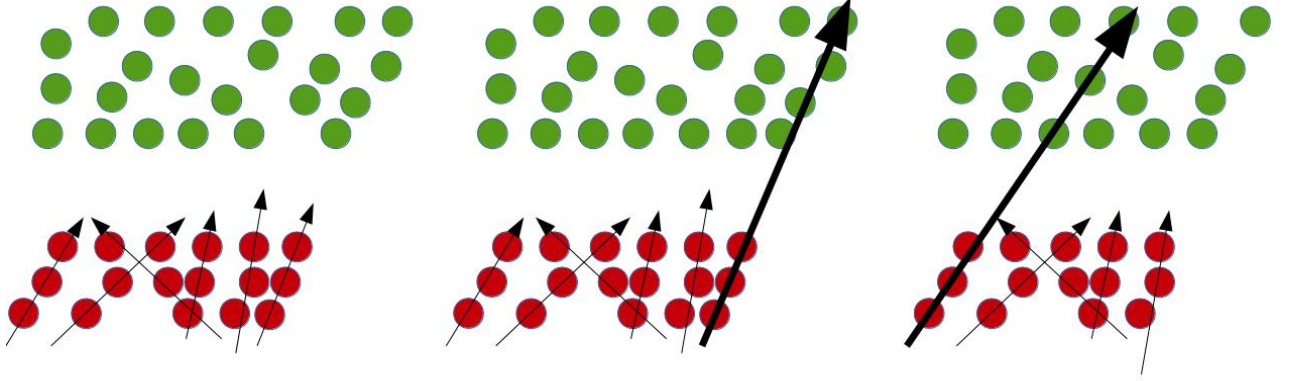


Figure 5.1: A visual depiction of the iterative tracking algorithm. First, pixel triplets (in red) are identified. Secondly, the best match of pixel hits and track hits is identified. Finally, the identified track is removed and the algorithm finds the second best track candidate.

Nuclear interactions in the tracker material can cause tracks to appear displaced. These interactions are identified by linking three tracks to a common secondary vertex. A secondary vertex is a vertex that is displaced from the primary vertex of the collision. A primary track is required to link the secondary vertex to the primary vertex. The tracks linked to the secondary vertex are required to have an invariant mass greater than 200 MeV.

After identifying the tracks, their positions are extrapolated to associate them with energy deposits in other parts of the detector. Due to the magnetic field, the radius of the track will depend on the particle's momentum. The momentum of the track is compared to the energy measured in the calorimeters or the muon system to determine if the track was associated with the deposit. In this way, tracks and calorimeter deposits are linked together to reconstruct each particle of the event. Each particle has its own unique reconstruction conditions, which are described below.

5.2 Electrons

Electrons are identified by associating tracks to objects known as "superclusters." As electrons interact with the detector, they will lose kinetic energy in the form of radiated photons. This is known as bremsstrahlung radiation [24]. These radiated photons are not affected by the magnetic field of CMS. As a result, the electron energy will be spread out in (η, ϕ) in the ECAL because the radiated photons are unaffected by the magnetic field.

Tracks from the standard iterative tracking procedure are used as electron candidates. Their p_T is required to be greater than 2 GeV. The electrons may not interact substantially with the detector, so if the track is propagated to the ECAL (Section 3.2.3) and if its p_T matches the ECAL cluster deposit, then the track is pre-identified as an electron. Otherwise the track is fit with a Gaussian-sum filter (GSF) to account for the non-Gaussian energy loss [1]. A boosted decision tree [27] is then used to select the final GSF electron track candidates.

Photons are neutral particles and will therefore not leave any tracks in the tracker. Bremsstrahlung photons are reconstructed by examining tangents to the tracks at each tracker layer, where the bremsstrahlung radiation may have occurred as the electrons passed through the layer. These tangent tracks are extrapolated to the ECAL. If any of the extrapolated bremsstrahlung photon tracks are associated with clusters in the ECAL then those ECAL clusters are considered part of the electron supercluster. A similar procedure is used to add clusters associated with bremsstrahlung photon e^+e^- pair production. Tracks associated with the supercluster have a high probability of being associated with jets or other particles. A more sophisticated method is needed to properly associate electron tracks with the supercluster. Tracks linked to cluster if extrapolated position overlaps with η/ϕ position of cluster.

The GSF electron tracks are then matched to an ECAL supercluster of at least 10 GeV. No more than 10% of the ECAL should be found in a topologically linked section of the HCAL. A boosted decision tree [27] takes as inputs the ECAL energy, HCAL energy, GSF track quality, among other parameters, and is trained to identify electrons. If there is no associated GSF track the particle flow candidate is defined as a photon. The reconstruction efficiency for electrons is about 90% for

$p_T > 20$ GeV. [29]

5.3 Muons

Muons are highly penetrating particles [33] that deposit a minimal amount of energy in the ECAL and HCAL before depositing the remainder of their energies in the muon system. The muon system is discussed further in Section 3.2.5.

Muons are identified in three different ways. Standalone muons are identified based on hits in the DT, CSC, and RPC elements of the muon system. Hits in the DT's and CSC's are used as a seeds for a KF fit of the DT, CSC, and RPC hits. The resulting track is defined as a standalone muon. [15] If a standalone muon track is matched to a tracker track, then the two tracks are combined using the KF technique to create a global muon track. At high $p_T > 200$ GeV global muons have improved momentum resolution compared to standalone muons.

Tracker muons are constructed by extrapolating all tracker tracks with $p_T > 0.5$ GeV and $p > 2.5$ GeV to the muon system. If the track matches a small segment of DT and CSC hits, the track is considered to be a tracker muon. Tracker muons improve efficiency for muons with low $p_T < 5$ GeV because low energy muons won't register enough hits in the muon system to be identified as standalone or global muons.

The muon algorithms are very efficient, with approximately 99% of muons successfully identified in the tracker or the muon system. [15] To reduce the fake rate due to hadrons punching through the calorimeters, global muons are required to be isolated, with no more than 10% of their energy measured by the calorimeters or the tracker inside a cone of $\Delta R < 0.3$. Additionally, charged hadrons may be reclassified as muons if there is a large discrepancy between their track p_T and the sum of their particle flow linked calorimeter deposits.

5.4 Hadrons

Hadrons are identified after the unique signatures of electrons, photons, and muons are already identified and removed from the list of remaining particle flow candidates. Neutral hadrons will

only deposit energy in the calorimeters, while charged hadrons have associated tracks. For charged hadrons, the uncertainty in p_T returned by the track fit must be smaller than the calorimeter energy resolution for charged hadrons, described in Sections 3.2.3 and 3.2.4. The hadronic deposits are used to reconstruct jets and hadronic tau decays.

5.4.1 Jets

After hadronic deposits are reconstructed via particle flow, the anti- k_t [13] algorithm is used to cluster the deposits and define jets. A distance metric between hadronic particles i and j is defined: $d_{ij} = \min(\frac{1}{k_{ti}^2}, \frac{1}{k_{tj}^2}) \frac{\Delta_{ij}^2}{R^2}$. Here k_t is the transverse momentum and $\Delta_{ij}^2 = (y_i - y_j)^2 + (\phi_i - \phi_j)^2$, where y and ϕ are the rapidity and azimuth of the particle, as defined in Chapter 2. At CMS, a radius of $R = 0.5(0.4)$ is used at 8 TeV (13 TeV). The distance between particle i and the beam is defined as $d_{iB} = \frac{1}{k_{ti}^2}$.

Beginning from a particle j , neighboring particles i are combined while $d_{ij} < d_{ib}$. Otherwise, i is considered the seed for a different jet. The results of this algorithm are shown in Figure 5.2. The anti- k_t algorithm is infrared safe and collinear safe [13] which means that the jet clustering process is not affected significantly by low energy soft radiation.

Charged hadron subtraction is used to reduce the dependence of the jets on pileup (Section 2.1). The majority of jet energy is carried by charged hadrons. For example, at $p_T = 100$ GeV charged hadrons are responsible for 65% of the jet energy. Photons carry 25% of the energy and neutral hadrons carry 10% of the energy. The charged hadron constituents of the jets still have track information stored via the particle flow algorithm. Any charged hadrons associated with pileup vertices instead of the primary vertex are retroactively removed from the jet. [31]

Additionally, three levels of corrections are applied to the jets. L1 corrections use the average p_T density per unit area to subtract energy associated with a combination of the underlying event, electronic noise, and pileup [31]. L2L3 corrections use Monte Carlo to calibrate the differences between reconstructed jets and generated jets in bins of p_T and η .

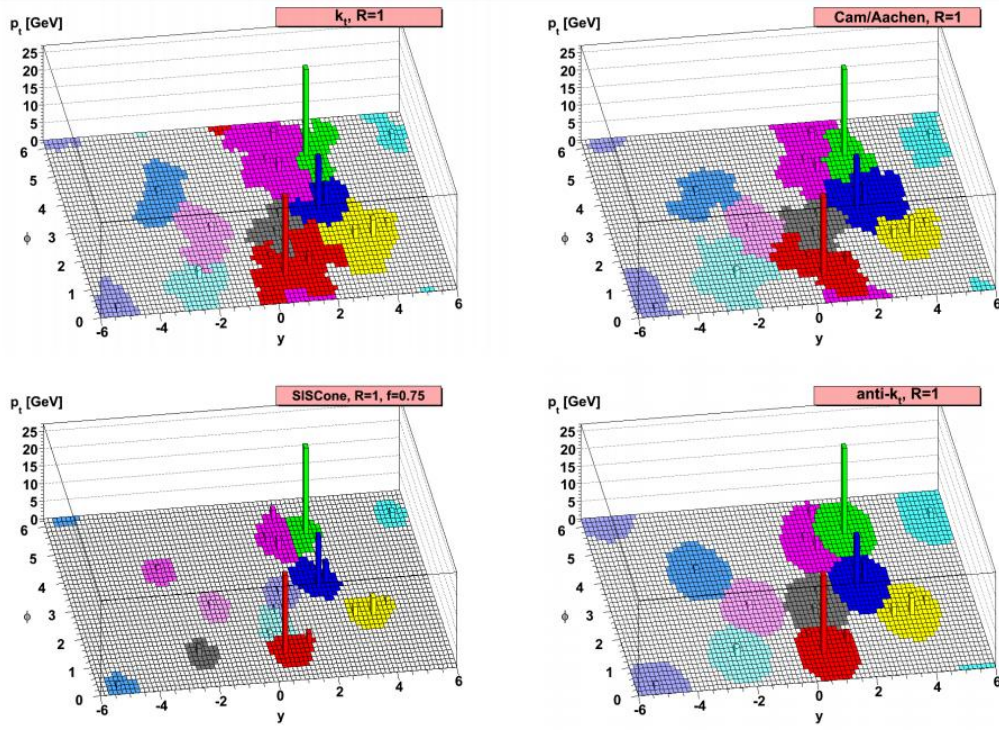


Figure 5.2: Performance of the anti- k_t algorithm. [13] Note that the anti- k_t algorithm is the only algorithm that generates a circular hard jet.

5.4.2 Taus

As discussed in Chapters 1 and 2, taus can decay leptonically to electrons or muons, or hadronically to quarks. Taus are identified separately depending on their decay products, so the identification of leptonic tau decays has already been discussed in Sections 5.3 and 5.4, which describe the identification of electrons and muons respectively. This section will discuss the identification of hadronic taus. As discussed in Chapter 2, taus can decay hadronically in three dominant ways: To a charged pion, to a charged pion and a neutral pion, or to three pions. These decays are referred to respectively as 0 prong, 1 prong, and 3 prong.

If the tau decays exclusively to charged hadrons, the hadronic tau (τ_h) is identified by comparing the invariant mass of the hadrons to the invariant mass of the tau. For example, if the tau decays to three charged pions, the invariant mass of the pion system must be between 0.8 GeV and 1.5 GeV, and the tracks must originate within $\Delta z < 0.4$ cm of the same event vertex [17], where Δz is the distance in the x-y plane of CMS, as discussed in Section 3.2.

If a neutral pion is involved in the hadronic tau decay, then the hadron plus strips (HPS) method must be used to identify the taus. Neutral pions convert to energetic photons in the tracker which then produce electron positron pairs. These particles will be bent in opposite directions in the magnetic field of CMS and will deposit their energy in the ECAL in a strip in ϕ . If a charged hadron from particle flow is linked to a strip in ECAL, and the invariant mass of the system is compatible with the hadronic tau mass, then the object is identified as a tau.

5.5 Missing Energy

There are some particles, for example neutrinos or dark matter candidates, that CMS cannot detect. They can be measured by applying the principle of conservation of energy. The transverse vector sum of all particle flow candidates in the event is computed. If CMS detected every particle, this sum would be zero. Therefore, the energy that CMS did not detect can be quantified by reversing the vector sum of the particles that were detected. If the jet energy corrections are included in the vector sum, the transverse missing energy (MET) is said to be Type 1 corrected [30]

Chapter 6

Analysis Methods: Summarize W+Jets and LFV Higgs ANs

6.1 Background Estimation

6.1.1 Monte Carlo Samples Used: This section will simply list the Monte Carlo samples used, in contrast with the Monte Carlo Generation section which will list the different Monte Carlo generator techniques.

8 TeV: The dominant backgrounds are estimated with data while the less significant backgrounds are estimated with simulations. The largest backgrounds come from $Z \rightarrow \tau\tau$ and from jets faking leptons in $W + jets$ and QCD multi-jet events. The $Z \rightarrow \tau\tau$ background is estimated using an embedding technique in which simulated tau decays replace the muons in $Z \rightarrow \mu\mu$ data. The misidentified lepton rates are measured in an independent data set and then applied to control regions to estimate the background.

13 TeV: The background contribution from $Z \rightarrow \tau\tau$ is estimated with simulation. The simulated events are corrected for residual discrepancies between data and simulation. These discrepancies, which are related to the lepton triggering, identification, and isolation, are determined from the tag-and-probe technique in $Z \rightarrow ll$ data [?, 29]. The background contribution coming from SM H decays in the $H \rightarrow \tau\tau$ channel is estimated with simulation. This background is suppressed by the kinematic selection criteria and peaks below 125 GeV. The W leptonic decay from $t\bar{t}$ produces opposite-sign dileptons and MET . In the $\mu\tau_e$ channel this background is estimated with simulated

$t\bar{t}$ events using the shape of the M_{col} distribution from simulation and a data control region for normalization. The control region is the 2-jet selection but with the additional requirement that at least one of the jets is b-tagged in order to enhance the $t\bar{t}$ contribution. Other backgrounds come from WW , ZZ , $W\gamma$ and single top-quark production. Each of these is estimated with simulation.

6.1.2 QCD Estimation

6.1.3 Tau Embedding

8 TeV pas The $Z \rightarrow \tau\tau$ background is estimated using a particle flow embedding technique. A sample of $Z \rightarrow \mu\mu$ events is taken from data using a loose selection. The muons are then replaced with simulated tau decays reconstructed with the particle flow algorithm. Thus the key features of the event topology such as the jets, missing energy and underlying event are taken directly from data with only the tau decays being simulated. The normalization of the sample is from the simulation expectation. The technique is validated by comparing identification efficiencies estimated with embedded decays to those from simulated $Z \rightarrow \tau\tau$ decays. It is found that the muon and hadronic tau efficiencies are well reproduced. There are small differences in the the electron identification efficiency. The differences are understood to be a consequence of the selective readout of the ECAL and corrections are applied for this.

6.1.4 Fake Rate Method

8 TeV:

Leptons can arise from misidentified jets from W +jets and QCD multi-jet events. This background is estimated using a data based method. It is employed slightly differently in the two channels. The technique is shown schematically in Table 6.2. The difference in the two channels is how the selection requirements are altered to define regions III and IV. In $H \rightarrow \mu\tau_e$ region I is the signal region in which an isolated muon and an isolated electron is required. Region III is a data sample in which all the analysis selection criteria are applied except that one of the leptons is required to be not-isolated, so that there are two components; isolated muon plus not-isolated electron events, and also isolated electron plus not-isolated muon events.

These samples are dominated by W +jets and QCD multi-jets but with small backgrounds from WW , ZZ that are subtracted using simulation expectations. The misidentified muon background in

Table 6.1: Schematic to illustrate the application of the method used to estimate the misidentified lepton background. Samples are defined by the charge of the two leptons and by the selection requirements on each. The selection requirement and charge requirement is altered on the second lepton to define four regions.

	Opposite Sign leptons	Same Sign leptons
Selection(lepton1), Selection*(lepton2)	Region III	Region IV
Selection(lepton1), Selection(lepton2)	Region I	Region II

Figure 6.1: Left) $M_{collinear}$ for the $H \rightarrow \mu\tau_e$ same sign isolated e or μ plus isolated μ or e sample (region II). Right) $M_{collinear}$ for the $H \rightarrow \mu\tau_{had}$ same sign isolated muon plus tight-isolated tau (region II).

region I is then estimated by multiplying the event yield in region III by a factor $f_\mu \cdot \epsilon_{trigger}$, where f_μ is the ratio of not-isolated to isolated muons. It is computed in an independent data sample $Z(\mu\mu) + (X = \mu)$

$$f_\mu = \frac{N_{events}(Z(\mu\mu) + \mu_{isolated})}{N_{events}(Z(\mu\mu) + \mu_{not-isolated})}.$$

in bins of muon p_T and η . A correction $\epsilon_{trigger}$ is made to account for the difference in trigger efficiency for selecting the isolated electron plus not-isolated muon versus selecting the isolated electron plus isolated muon. It is computed by selecting data in an independent single electron triggered data sample, applying the full event selection and then taking the ratio of the number of events that pass the electron-muon cross-trigger from the isolated versus not-isolated sample. The misidentified electron background is computed in exactly the same way. The technique is validated by using a like-sign rather than opposite-sign data sample in the same way as shown schematically in Table 6.2. Like sign leptons are chosen rather than opposite sign. Figure 6.2 shows the measured versus predicted by simulation $M_{collinear}$ distribution for the like sign control region. The agreement is very good.

In the $H \rightarrow \mu\tau_{had}$ channel tau leptons can be misidentified jets arising from a number of sources. Predominantly W +jets and QCD multi-jet events, but also $Z(\mu\mu)$ +jets, $t\bar{t}$ +jets. The misidentification rate f_τ is measured in $Z(\mu\mu) + X = (\tau)$ events. It is defined as

$$f_\tau = \frac{N_{events}(Z(\mu\mu) + X = (\tau, ID + tight - isolated))}{N_{events}(Z(\mu\mu) + X = (\tau, ID + loose - isolated))}.$$

The denominator is the number of events with an object identified as a τ except that the requirement on isolation is loosened. The numerator is the number of events where the normal tau isolation

(tight-isolated) requirement is made. The misidentification rate measured in $Z(\mu\mu) + X = (\tau)$ data is checked by comparing to that measured in $Z(\mu\mu) + X = (\tau)$ simulation and found to be in good agreement. The measured misidentification rate is then used in the same way as previously described, and illustrated schematically in Figure 6.2. In this case region I, the signal region is the baseline event selection with both an isolated tau and an isolated muon. Region III comprises the baseline selection with an isolated muon and a *loose-isolated* & *not-tight-isolated* tau requirement. This region is dominated by W +jets and QCD multi-jet background and there good agreement between the data and the expected yields from simulation. The isolated muon plus *loose-isolated* & *not-tight-isolated* tau region is then used to estimate the misidentified lepton background using the following relation:

$$\frac{N_{events}(\tau_{tight-isolated})}{N_{events}(\tau_{loose-isolated.\&.not-tight-isolated})} = \frac{f_{\tau} N_{events}(\tau ID)}{(1 - f_{\tau}) N_{events}(\tau ID)}.$$

Hence the background in the signal region (region I) is given by

$$N_{events}(\tau_{tight-isolated}) = \frac{f_{\tau}}{(1 - f_{\tau})} N_{events}(\tau_{loose-isolated.\&.not-tight-isolated}).$$

The procedure can be validated with like sign $\mu\tau$ events. Figure 6.2 shows the excellent agreement between data and simulation for the like sign samples. As an additional test, the method is tested on opposite sign $\mu\tau$ events, with tight isolation applied to the tau, after the pre-selection and without the requirements on the kinematic variables. Again there is excellent agreement between data and simulation for this region.

The method assumes that the misidentification rate in $Z(\mu\mu) + X = (\tau)$ events is the same as for W +jets and QCD processes. To test this assumption the misidentification rates are measured in a QCD data control sample. They are found to be consistent, but slightly lower. A conservative 30% uncertainty is assigned. Finally as a cross-check the study has been performed also as a function of the number of jets in the event and similar agreement found.

13 TeV: The largest backgrounds come from $Z \rightarrow \tau\tau$ and from misidentified leptons in W +jets and QCD multijet production. The contribution of the misidentified lepton background is estimated using data, while the remaining backgrounds are estimated using simulation. The simulated backgrounds are normalized by applying a scale factor equal to the ratio of the observed luminosity in data to the effective luminosity of the simulated sample.

Reconstructed leptons can arise from misidentified jets in W +jets and QCD multijet processes. This background is estimated with data. A sample with similar kinematic properties to the signal

sample but enriched in W +jets and QCD multijets is defined. Then the probability for objects to be misidentified as leptons is measured in an independent data set, and this probability is applied to the enriched sample to compute the misidentified lepton background in the signal region. The technique is shown schematically in Table 6.2 in which four regions are defined including the signal and background enriched regions (I and III) and two control regions (II and IV) used for validation of the technique. It is employed slightly differently in the $H \rightarrow \mu\tau_e$ and $H \rightarrow \mu\tau_h$ channels because the lepton isolation requirements used to define the enriched regions in each channel are slightly different.

In the $H \rightarrow \mu\tau_e$ channel, region I is the signal region in which an isolated μ and an isolated e are required. In region III all the analysis selection criteria are applied to the data sample except that one of the leptons is required to be not-isolated. This creates a misidentified lepton rich region. There are two types of events in this region: events with an isolated μ and not-isolated e events, as well as events with an isolated e and not-isolated μ events. There is negligible number of signal events in region III. Regions II and IV are data samples formed with the same selection criteria as regions I and III, respectively, but with same-sign rather than opposite-sign leptons. The kinematic distributions of the same-sign samples are very similar to the opposite-sign samples

Table 6.2: Definition of the samples used to estimate the misidentified lepton (ℓ) background. They are defined by the charge of the two leptons and by the isolation requirements on each.

Opposite sign leptons	Like sign leptons
Region I	Region II
$\ell_1^\pm(\text{isolated})$	$\ell_1^\pm(\text{isolated})$
$\ell_2^\mp(\text{isolated})$	$\ell_2^\pm(\text{isolated})$
Region III	Region IV
$\ell_1^\pm(\text{isolated})$	$\ell_1^\pm(\text{isolated})$
$\ell_2^\mp(\text{not-isolated})$	$\ell_2^\pm(\text{not-isolated})$

The sample in region III is dominated by W +jets and QCD multijets but with small contributions from WW , ZZ and WZ that are subtracted using simulation. The misidentified e background in region I is then estimated by multiplying the event yield in region III by a factor f_e , where f_e is the ratio of not-isolated to isolated e 's. It is computed in an independent data sample $Z \rightarrow \mu\mu + X$, where X is an object identified as a e , in bins of p_T and η .

$$f_e = \frac{N_{events}(Z \rightarrow \mu\mu + e_{isolated})}{N_{events}(Z \rightarrow \mu\mu + e_{non-isolated})} \quad (6.1)$$

The $Z \rightarrow \mu\mu + X$ sample is corrected for contributions from WW , ZZ and WZ using simulated

samples. The misidentified μ background is computed in exactly the same way. The technique is validated by using the same-sign data from regions II and IV as shown schematically in Table 6.2. In Fig. 6.2(left) the observed data yield in region II is compared to the estimate from scaling the region IV sample by the measured misidentification rates. The region II sample is dominated by misidentified leptons but also includes small contributions of true leptons arising from vector boson decays, estimated with simulated samples.

In the $H \rightarrow \mu \tau_h$ channel, the τ_h candidate can come from a misidentified jet with a number of sources, predominantly W +jets and QCD multijets, but also $Z \rightarrow \mu\mu$ +jets and $t\bar{t}$. In this case the enriched background regions are defined with τ_h candidates that pass a looser isolation requirement, but do not pass the signal isolation requirement. The misidentification rate f_{τ_h} is then defined as the fraction of τ_h candidates with the looser isolation that also pass the signal isolation requirement. It is measured in observed $Z \rightarrow \mu\mu + X$ events, where X is an object identified as a τ_h .

$$f_{\tau} = \frac{N_{events}(Z \rightarrow \mu\mu + X = (\tau, ID + tight - isolated))}{N_{events}(Z \rightarrow \mu\mu + X = (\tau, ID + loose - isolated))} \quad (6.2)$$

The misidentification rate measured in $Z \rightarrow \mu\mu + X$ data is checked by comparing to that measured in $Z \rightarrow \mu\mu + X$ simulation and found to be in good agreement. The differences observed between different decay modes of the τ_h candidate are taken into account in the analysis.

The misidentified background in the signal region (region I) is estimated by multiplying the event yield in region III by a factor $f_{\tau_h}/(1 - f_{\tau_h})$. The procedure is validated with same-sign $\mu\tau$ events in the same way as for the $H \rightarrow \mu\tau_e$ channel above. Figure 6.2 (right) shows the data in region II compared to the estimate from scaling region IV by the misidentification rates.

Figure 6.2: Distributions of M_{col} for region II compared to the estimate from scaling the region IV sample by the measured misidentification rates. The bottom panel in each plot shows the fractional difference between the observed data and the estimate. Left: $H \rightarrow \mu\tau_e$. Right: $H \rightarrow \mu\tau_h$.

6.2 Selection Optimization

8 TeV:

The event selection consists of three steps. First a loose pre-selection defining the basic signature. The sample is then divided into categories. Finally requirements are placed on a set of kinematic variables designed to suppress the backgrounds.

The pre-selection for the $H \rightarrow \mu\tau_e$ sample requires an isolated tight muon ($p_T > 25$ GeV, $|\eta| < 2.1$) and an isolated tight electron ($p_T > 10$ GeV, $|\eta| < 2.3$) of opposite charge lying within a region of the detector that allows good identification. The $H \rightarrow \mu\tau_{had}$ sample requires an isolated muon ($p_T > 30$ GeV, $|\eta| < 2.1$) and a tightly isolated hadronic tau ($p_T > 30$ GeV, $|\eta| < 2.3$) of opposite charge.

The events are then divided into categories within each sample according to the number of jets in the event. Jets are required to pass loose identification criteria, have $p_T > 30$ GeV and lie within the range $|\eta| < 4.7$. The zero jet category contains events primarily produced by gluon-gluon fusion. The one jet category contains events produced by gluon-gluon fusion but also events produced in association with a W or Z boson decaying hadronically. Events enhanced in the vector boson fusion process are required to have two jets separated by a rapidity gap ($\Delta\eta > 3.5$) and to have an invariant jet-jet mass greater than 550 GeV. In the $H \rightarrow \mu\tau_e$ channel events in which at least one of the jets is identified as coming from a b-quark decay are vetoed.

Table 6.3: Selection criteria requirements for the kinematic variables after pre-selection.

Variable	$H \rightarrow \mu\tau_e$			$H \rightarrow \mu\tau_{had}$		
	0-jet	1-jet	2-jet	0-jet	1-jet	2-jet
$p_T^\mu > [\text{GeV}]$	50	45	25	40	35	30
$p_T^e > [\text{GeV}]$	10	10	10	-	-	-
$p_T^\tau > [\text{GeV}]$	-	-	-	35	40	40
$\Delta\phi_{\bar{\mu}-\tau_{had}} >$	-	-	-	2.7	-	-
$\Delta\phi_{\bar{e}-MET} <$	0.5	0.5	0.3	-	-	-
$\Delta\phi_{\bar{e}-\bar{\mu}} >$	2.7	1.0	-	-	-	-
$M_T(e) < [\text{GeV}]$	65	65	25	-	-	-
$M_T(\mu) > [\text{GeV}]$	50	40	15	-	-	-
$M_T(\tau) < [\text{GeV}]$	-	-	-	50	35	35

The signal variable is the collinear mass, $M_{collinear}$, which provides an estimator of the reconstructed Higgs mass using the observed decay products. This is constructed using the collinear approximation [?] which is based on the observation that since the mass of the Higgs is much greater than the mass of tau, the tau decay products are highly boosted in the direction of the original tau. Thus the neutrino momenta can be approximated to be in the same direction as the other visible decay products of the tau. Hence the component of the missing transverse energy in the direction of the visible tau decay products is used to estimate the transverse component of the

neutrino momentum:

$$\vec{p}_T^\nu = M\vec{E}T \cdot \hat{p}_T^{\tau_{vis}}$$

The fraction of the tau momentum carried by the visible tau decay products, $x_{\tau_{vis}}$, is given by

$$x_{\tau_{vis}} = \frac{|\vec{p}_T^{\tau_{vis}}|}{|\vec{p}_T^{\tau_{vis}}| + |\vec{p}_T^\nu|}$$

The tau four momentum is then $(x_{\tau_{vis}}|\vec{p}_T^{\tau_{vis}}|, x_{\tau_{vis}}\vec{p}_T^{\tau_{vis}})$ and since $M_H \gg m_\tau^2, m_l^2$

$$M_H = M_{collinear} = \frac{M_{vis}}{\sqrt{x_{\tau_{vis}}}}.$$

Figure 6.4 shows $M_{collinear}$ for the background regions compared to data for each of the categories in each channel after the pre-selection. The signal simulation for $B(H \rightarrow \mu\tau) = 100\%$ is shown. The principle backgrounds are estimated with data using techniques described in section ?? . There is excellent agreement between data and the background estimation. The agreement is similarly good in all of the kinematic variables that are subsequently used to suppress backgrounds. The analysis was performed “blinded” in the region $100\text{GeV} < M_{collinear} < 150\text{GeV}$.

Figure 6.3: The collinear mass $M_{collinear}$ for signal ($B(H \rightarrow \mu\tau) = 100\%$ for clarity) and background after pre-selection requirements for the LFV $H \rightarrow \mu\tau$ decays for the different channels and categories compared to data. The shaded grey bands indicate the uncertainty. Top left: $H \rightarrow \mu\tau_e$ 0-jet , top right: $H \rightarrow \mu\tau_{had}$ 0-jet, middle left: $H \rightarrow \mu\tau_e$ 1-jet, middle right: $H \rightarrow \mu\tau_{had}$ 1-jet, bottom left: $H \rightarrow \mu\tau_e$ 2-jet, bottom right $H \rightarrow \mu\tau_{had}$ 2-jet.

Next, a set of kinematic variables is defined and the criteria for selection is determined by optimizing for $S/\sqrt{S+B}$ where S and B are the expected signal and background event yields in the mass window $100\text{ GeV} < M_{collinear} < 150\text{ GeV}$. The signal strength is set according to the standard model Higgs production cross-section at $M_H = 126\text{GeV}$ with $B(H \rightarrow \mu\tau) = 10\%$. This value for the LFV Higgs branching fraction is chosen because it corresponds to the limit from indirect measurements as described in reference [26]. The criteria for each category, and in each channel, are given in Table 6.5. The variables used are; the transverse momenta of the tau, muon and electron objects; azimuthal angles between the leptons, azimuthal angles between the leptons and the transverse missing energy vector, and finally the transverse mass. The transverse mass is constructed from the transverse missing energy vector $M\vec{E}T$ and the lepton vector \vec{l} as follows:

$$M_T(l) = \sqrt{2p_T(l)M\vec{E}T(1 - \cos \Delta\phi_{\vec{l}-M\vec{E}T})}$$

Table 6.4: Selection criteria for the kinematic variables after the loose selection.

Variable [GeV]	$H \rightarrow \mu\tau_e$			$H \rightarrow \mu\tau_h$		
	0-jet	1-jet	2-jet	0-jet	1-jet	2-jet
$p_T^\mu >$	50	45	25	45	35	30
$p_T^e >$	10	10	10	NA	NA	NA
$p_T^{\mu\tau_h} >$	NA	NA	NA	35	40	40
$M_T^e <$	65	65	25	NA	NA	NA
$M_T^\mu >$	50	40	15	NA	NA	NA
$M_T^{\mu\tau_h} <$	NA	NA	NA	50	35	35
[radians]						
$\Delta\phi_{\vec{p}_T^\mu - \vec{p}_T^{\mu\tau_h}} >$	NA	NA	NA	2.7	NA	NA
$\Delta\phi_{\vec{p}_T^e - \vec{M}\vec{E}T} <$	0.5	0.5	0.3	NA	NA	NA
$\Delta\phi_{\vec{p}_T^e - \vec{p}_T^\mu} >$	2.7	1.0	NA	NA	NA	NA

13 TeV: The event selection consists of three steps. First, a loose selection defining the basic signature is applied. The sample is then divided into categories, according to the number of jets in the event. Finally, requirements are placed on a set of kinematic variables designed to suppress the backgrounds.

The loose selection for the $H \rightarrow \mu\tau_e$ channel requires an isolated μ ($p_T > 25\text{GeV}$, $|\eta| < 2.1$) [?] and an isolated e ($p_T > 10\text{GeV}$, $|\eta| < 2.3$) [29] of opposite charge lying within a region of the detector that allows good identification. The e and μ are required to be separated by $\Delta R > 0.1$, where ΔR is a distance metric defined as $\sqrt{\Delta\phi^2 + \Delta\eta^2}$. The $H \rightarrow \mu\tau_h$ channel requires an isolated μ ($p_T > 30\text{GeV}$, $|\eta| < 2.1$) and an isolated hadronically decaying τ ($p_T > 30\text{GeV}$, $|\eta| < 2.3$) [?] of opposite charge. Leptons are required to be separated from any jet in the event with $p_T > 30\text{GeV}$ by $\Delta R > 0.4$ and to have an impact parameter consistent with the primary vertex.

The events are then divided into categories within each channel according to the number of jets in the event. Jets are constructed via the anti-kt algorithm [13] with a distance metric of $\Delta R < 0.4$. Jets are required to pass identification criteria [?], have $p_T > 30\text{GeV}$ and lie within the range $|\eta| < 4.7$. The zero and one jet categories contains signal events predominantly produced by gluon-gluon fusion, and the two jet category is enriched with signal events produced by vector boson fusion.

A set of kinematic variables is defined and the criteria for selection were determined at 8 TeV by optimizing for $S/\sqrt{S+B}$ where S and B are the expected signal and background event yields in the mass window $100 < M_{\text{col}} < 150\text{GeV}$ [?]. The variable M_{col} refers to the collinear mass, which provides an estimate of M_H using the observed decay products. It is constructed using the

collinear approximation based on the observation that since $M_H \gg M_\tau$, the τ decay products are highly Lorentz boosted in the direction of the τ [?]. The neutrino momenta can be approximated to have the same direction as the other visible decay products of the τ (τ^{vis}) and the component of the $M\vec{E}T$ in the direction of the visible τ decay products is used to estimate the transverse component of the neutrino momentum ($p_T^{\nu, \text{est}}$). M_{col} can be then derived from the visible mass of the $\tau - e$ system (M_{vis}) as $M_{\text{col}} = M_{\text{vis}} / \sqrt{x_\tau^{\text{vis}}}$, where x_τ^{vis} is the fraction of energy carried by the visible decay products of the τ ($x_\tau^{\text{vis}} = p_T^{\tau^{\text{vis}}} / (p_T^{\tau^{\text{vis}}} + p_T^{\nu, \text{est}})$).

This 13 TeV analysis reuses the same optimization but loosens the criteria in the two jet category because of the reduced statistics of the 2015 data sample. The selection criteria for each category, and in each channel, are given in Table 6.5. The variables used are the lepton transverse momenta p_T^ℓ with $\ell = \text{muon}, \mu, e$; azimuthal angles between the leptons $\Delta\phi_{p_T^{\ell_1} - p_T^{\ell_2}}$; azimuthal angle $\Delta\phi_{p_T^\ell - M\vec{E}T}$; the transverse mass $M_T^\ell = \sqrt{2p_T^\ell E_T^{\text{miss}}(1 - \cos \Delta\phi_{p_T^\ell - E_T^{\text{miss}}})}$. Events in the 2-jet category are required to have exactly two jets with large dijet invariant mass separated by a pseudorapidity gap.

In the $H \rightarrow \mu\tau_e$ channel events in which at least one of the jets identified as coming from a b-quark decay are using the combined secondary-vertex b-tagging algorithm [?] are vetoed, to suppress backgrounds from top quark decays.

Table 6.5: Signal region definition

Variable	$H \rightarrow \mu\tau_e$			$H \rightarrow \mu\text{muon}\tau_h$		
	0-jet	1-jet	2-jet	0-jet	1-jet	2-jet
$p_T^\mu > [GeV]$	50	45	25	45	35	40
$p_T^e > [GeV]$	15	15	15	NA	NA	NA
$p_T^{\text{muon}\tau_h} > [GeV]$	NA	NA	NA	35	40	40
$M_T^e < [GeV]$	65	65	40	NA	NA	NA
$M_T^\mu > [GeV]$	50	40	15	NA	NA	NA
$M_T^{\text{muon}\tau_h} < [GeV]$	NA	NA	NA	50	35	35
$\Delta\phi_{p_T^\mu - p_T^{\text{muon}\tau_h}} >$	NA	NA	NA	2.7	NA	NA
$\Delta\phi_{p_T^e - M\vec{E}T} <$	0.5	0.5	NA	NA	NA	NA
$\Delta\phi_{p_T^e - p_T^\mu} >$	2.7	1.0	NA	NA	NA	NA
VBF dijet $ \Delta\eta >$	NA	NA	2.5	NA	NA	2.5
VBF dijet mass $> [GeV]$	NA	NA	200	NA	NA	200

The main observable used to discriminate between the signal and the background is the collinear mass, M_{col} .

Figure 6.4 shows M_{col} distribution for the signal and background compared to data for each of the categories in each channel after the loose selection. The simulated signal for $\mathcal{B}(H \rightarrow \mu\tau) = 100\%$ is

shown. The principal backgrounds are estimated with data using techniques described in Section ??.

There is good agreement between data and the background estimation.

Figure 6.4: Distributions of the collinear mass M_{col} for signal with $\mathcal{B}(H \rightarrow \mu\tau) = 100\%$ for clarity, and background processes after the loose selection requirements for the LFV $H \rightarrow \mu\tau$ candidates for the different channels and categories compared to data. The shaded grey bands indicate the total uncertainty. The bottom panel in each plot shows the fractional difference between the observed data and the total estimated background. Top left: $H \rightarrow \mu\tau_e$ 0-jet; top right: $H \rightarrow \mu\tau_h$ 0-jet; middle left: $H \rightarrow \mu\tau_e$ 1-jet; middle right: $H \rightarrow \mu\tau_h$ 1-jet; bottom left: $H \rightarrow \mu\tau_e$ 2-jet; bottom right $H \rightarrow \mu\tau_h$ 2-jet.

6.2.1 W+Jets

6.2.2 LFV Higgs

6.3 Systematic Uncertainties

6.3.1 W+Jets

6.3.2 LFV Higgs

8 TeV: The presence or absence of a signal is established using the asymptotic CL_s method ^{**citeLHC-HCG-Report**}. Shape templates of $M_{\text{collinear}}$ distributions for the various background sources are used. The expected signal and background is then binned in $M_{\text{collinear}}$ and a likelihood technique is used to estimate the signal strength μ which in turn can be used to set confidence limits in the absence of a signal. The systematic uncertainties that are independent of $M_{\text{collinear}}$ are treated as “nuisance” parameters. There are also uncertainties that are dependent on $M_{\text{collinear}}$ which are estimated by changing the shape of the $M_{\text{collinear}}$ templates.

The systematic errors are summarized in Tables 6.12 and 6.9. The uncertainty in the electron and muon selection (trigger, identification and isolation) are estimated using the tag and probe technique in $Z(\mu\mu, ee)$ data. The hadronic tau efficiency is estimated using tag and probe in $Z(\tau\tau)$ data. The uncertainty in the $Z(\tau\tau)$ background comes predominantly from the uncertainty in the tau efficiency. The uncertainties in the estimation of the misidentified lepton rate come from the difference in rates measured in different data samples (QCD multi-jet and W +jets). The uncertainty

Table 6.6: Systematics. All systematics are treated as correlated between the categories, except where there are two numbers. In this case the number denoted with * is treated as uncorrelated between categories.

Systematic Uncertainty	$H \rightarrow \mu\tau_e$			$H \rightarrow \mu\tau_{had}$		
	0-jet	1-jet	2-jet	0-jet	1-jet	2-jet
electron trigger/ID/isolation	3%	3%	3%	-	-	-
muon trigger/ID/isolation	2%	2%	2%	2%	2%	2%
hadronic tau efficiency	-	-	-	9%	9%	9%
luminosity	2.6%	2.6%	2.6%	2.6%	2.6%	2.6%
$Z \rightarrow \tau\tau$ background	3+3*	3+5*	3+10*	3+5*	3+5*	3+10*
$Z \rightarrow \mu\mu, ee$ background	30%	30%	30%	30%	30%	30%
misidentified muon and electron background	40%	40%	40%	-	-	-
misidentified hadronic tau background	-	-	-	30+10*	30%	30%
WW, ZZ +jets background	15%	15%	15%	15%	15%	65%
$t\bar{t}$ +jets background	10 %	10 %	10+10*	10 %	10 %	10+33*
$W + \gamma$ background	100 %	100 %	100 %	-	-	-
B-tagging veto	3%	3%	3%	-	-	-
Single top production background	10 %	10 %	10 %	10 %	10 %	10%

Table 6.7: Systematic uncertainties in the expected event yield in %. All uncertainties are treated as correlated between the categories, except where there are two numbers. In this case the number denoted with * is treated as uncorrelated between categories and the total uncertainty is the sum in quadrature of the two numbers.

Systematic uncertainty	$H \rightarrow \mu\tau_e$			$H \rightarrow \mu\tau_{had}$		
	0-Jet	1-Jet	2-Jets	0-Jet	1-Jet	2-Jets
electron trigger/ID/isolation	3	3	3	NA	NA	NA
muon trigger/ID/isolation	2	2	2	2	2	2
hadronic tau efficiency	NA	NA	NA	9	9	9
luminosity	2.6	2.6	2.6	2.6	2.6	2.6
$Z \rightarrow \tau\tau$ background	3+3*	3+5*	3+10*	3+5*	3+5*	3+10*
$Z \rightarrow \mu\mu, ee$ background	30	30	30	30	30	30
misidentified μ, e background	40	40	40	NA	NA	NA
misidentified $\mu\tau_h$ background	NA	NA	NA	30+10*	30	30
WW, ZZ +jets background	15	15	15	15	15	65
$t\bar{t}$ background	10	10	10+10*	10	10	10+33*
$W + \gamma$ background	100	100	100	NA	NA	NA
b-tagging veto	3	3	3	NA	NA	NA
single top production background	10	10	10	10	10	10

in the production cross-section of the backgrounds that have been estimated by simulation is also included.

There are several uncertainties that arise from the theoretical uncertainty in Higgs production cross-section which differ for each production mechanism contribution within each category. They are given in Table 6.9. Note that these enter both for the LFV Higgs and the SM Higgs background and are treated as 100% correlated.

Table 6.8: Theoretical Uncertainties in Higgs production.

Uncertainty	Gluon-Gluon Fusion			Vector Boson Fusion		
	0-jet	1-jet	2-jet	0-jet	1-jet	2-jet
parton density function	+9.7%	+9.7%	+9.7%	+ 3.6%	+3.6%	+3.6%
renormalization scale	+8 %	+10 %	-30%	+4 %	+1.5%	+2%
underlying event/parton shower	+4%	-5%	-10%	+10%	0%	-1%

Table 6.9: Theoretical uncertainties in % for Higgs boson production. Anticorrelations arise due to migration of events between the categories and are expressed as negative numbers.

Systematic uncertainty	Gluon-Gluon Fusion			Vector Boson Fusion		
	0-Jets	1-Jets	2-Jets	0-Jet	1-Jet	2-Jets
parton distribution function	+9.7	+9.7	+9.7	+3.6	+3.6	+3.6
renormalization/factorization scale	+8	+10	-30	+4	+1.5	+2
underlying event/parton shower	+4	-5	-10	+10	<1	-1

The shape uncertainties are summarized in Table 6.11.

Table 6.10: Systematic uncertainties in % for the shape of the signal and background templates.

Systematic uncertainty	$H \rightarrow \mu\tau_e$	$H \rightarrow \mu\tau_{had}$
hadronic tau energy scale	NA	3
jet energy scale	3-7	3-7
unclustered energy scale	10	10
$Z \rightarrow \tau\tau$ bias	100	NA

Table 6.11: Systematic uncertainties in the shape of the signal and background templates.

Systematic	$H \rightarrow \mu\tau_e$	$H \rightarrow \mu\tau_{had}$
Hadronic Tau energy scale	-	3%
Jet Energy scale	3-7%	3-7%
Unclustered energy scale	10%	10 %
$Z(\tau\tau)$ Bias	100%	-

For the embedded $Z(\tau\tau)$ $M_{collinear}$ distribution a 1% shift has been observed with respect to $Z(\tau\tau)$ simulations by comparing the means of both templates. This occurs only in the $H \rightarrow \mu\tau_e$ channel. The template has been corrected for this effect and a 100% uncertainty on this shift is used.

The jet energy scale has been studied extensively by the CMS collaboration and a standard prescription is used in all analysis. The uncertainties are applied as a function of p_T and η including all correlations. The overall scale is set using $\gamma + \text{jets}$ events and the most significant uncertainty

is in the photon energy scale. A number of other uncertainties such as jet fragmentation modeling, single pion response and uncertainties in the pileup corrections are also included. The jet energy scale uncertainties are propagated to the missing energy. There is also an additional uncertainty added to account for the unclustered energy scale uncertainty. The unclustered energy comes from jets below 10 GeV and particle flow candidates not within jets. It also is propagated to the missing energy.

The tau energy scale is estimated by comparing $Z(\tau\tau)$ events in data and simulation. Good agreement is found and a 3% uncertainty is assigned. Finally the shape templates have a bin by bin statistical uncertainty that is also included.

Potential uncertainties in the shape of the misidentified lepton backgrounds have also been considered. The procedure for estimating the misidentified lepton contributions is described in Section ???. In the $H \rightarrow \mu\tau_e$ channel the misidentified lepton rates are applied in bins of p_T and η . These rates are adjusted all up or down by 1 standard deviation and the different shapes are then used as nuisance parameters in the fit.

In the $H \rightarrow \mu\tau_{had}$ channel the tau lepton misidentification rate was found to be approximately flat in p_T and η . To estimate the systematic uncertainty the p_T distribution is fit with a linear function and the rate recomputed from the fitted slope and intercept. The modified shape template is then used to compute the systematic uncertainty.

13 TeV: To set upper bounds on the signal strength we use the CL_s method [?, ?]. A binned likelihood is used, based on the distributions of M_{col} for the signal and the various background sources. Systematic uncertainties are represented by nuisance parameters, some of which only affect the background and signal normalizations, while others affect the shape and/or normalization of the M_{col} distributions.

The uncertainties in the electron and muon selections (trigger, identification, and isolation) are estimated using the tag and probe technique in $Z \rightarrow \mu\mu, ee$ data. The hadronic tau efficiency is estimated using tag and probe in $Z \rightarrow \tau\tau$ data. The uncertainty on the hadronic tau efficiency is used to estimate the uncertainty on the $Z \rightarrow \tau\tau$ background. The misidentified $\mu, e, \text{ and } \tau_h$ uncertainties are estimated from the agreement with data in a control region (region II).

The jet energy scale uncertainty is computed for each background by calculating the differences in yield and shape when the jet energy scale is altered by $\pm\sigma$, which results in a shift of 5% to 10% in jet p_T . A similar variation of the hadronic tau energy scale is used to calculate its uncertainties

Table 6.12: Systematic uncertainties in the expected event yield in %. All uncertainties are treated as correlated between the categories, except where there are two values. In this case the first value is correlated as above, while the second value (following \oplus) represents an uncorrelated uncertainty for each individual category. The total uncertainty in a given category is the sum in quadrature of the two values.

Systematic uncertainty	$H \rightarrow \mu\tau_e$	$H \rightarrow \mu\tau_h$
Muon trigger/ID/isolation	3%	3%
Electron trigger/ID/isolation	3%	NA
Hadronic tau efficiency	NA	10%
b-tagging veto	3%	NA
$Z \rightarrow \tau\tau$ background	$10\% \oplus 5\%$	$10\% \oplus 5\%$
$Z \rightarrow \mu\mu, ee$ background	$10\% \oplus 5\%$	$10\% \oplus 5\%$
Misidentified μ, e background	$40\% \oplus 10\%$	NA
Misidentified τ_h background	NA	$30\% \oplus 10\%$
WW, ZZ background	$10\% \oplus 5\%$	$10\% \oplus 5\%$
$t\bar{t}$ background	$20\% \oplus 5\%$	$20\% \oplus 5\%$
$W + \gamma$ background	$10\% \oplus 5\%$	NA
Single top production background	10%	10%
Jet energy scale	3-20%	3-20%
Hadronic tau energy scale	NA	3%
Misidentified lepton shape	$\pm\sigma$	$\pm\sigma$
Theory uncertainty	10%	10%
Luminosity	2.7%	2.7%

in yield and shape. A misidentified lepton shape uncertainty is computed by varying the lepton fake rate factors by $\pm\sigma$ and reapplying the fake rate method.

The theoretical uncertainties are calculated by adding the change in acceptance when the factorization and renormalization scales are shifted by a factor of two to the uncertainty in the Higgs production cross sections.

The uncertainties are summarized in Table 6.12.

Chapter 7

Results

7.1 LFV Higgs

7.1.1 Statistical Methods

7.1.1.1 Maximum Likelihood Fit

After selecting events which pass the signal region selections and defining sources of systematic uncertainty, the next step is to fit the backgrounds to the data. This is done via a binned maximum likelihood fit.[11][18] We assume that the number of events in each bin follows a Poisson distribution, defined as $P(n_i|\mu_i) = \frac{\mu_i^{n_i} e^{-\mu_i}}{n_i!}$, where n_i is the number of events in the i^{th} bin and μ_i is the number of Monte Carlo events in each bin.

We then define the likelihood L as $L = \prod P(n_i|\mu_i)$. The goal of the fit is to determine the μ_i that maximizes the likelihood. This procedure is complicated by the addition of the systematic uncertainties, which are treated as nuisance parameters. For example, the luminosity uncertainty introduces a 2.3% uncertainty. To account for this, each term in the likelihood expression is multiplied by a log-normal distribution. The log-normal distribution is used instead of the Gaussian distribution to prevent the parameter from becoming negative. The lognormal distribution is defined: $N(\mu, \sigma) = \frac{1}{x\sigma\sqrt{2\pi}} e^{-\frac{(\log x - \mu)^2}{2\sigma^2}}$. Shape uncertainties, like the jet energy scale and tau energy scale systematics, are represented by Gaussian distributions. For the j^{th} sample in the i^{th} bin we can write: $\epsilon_{ji} = \epsilon_{ji}^0 + f \frac{\epsilon_{ji}^+ - \epsilon_{ji}^-}{2}$. Here, ϵ_{ji}^0 is the efficiency before the shift, ϵ_{ji}^+ is the efficiency after the scale shift up, and ϵ_{ji}^- is the efficiency after the scale shift down. The morphing parameter f has a gaussian distribution. We can interpolate quadratically for $|f| < 1$ and write

$\epsilon_{ji} = \frac{f(f-1)}{2}\epsilon_{ji}^- - (f-1)(f+1)\epsilon_{ji}^0 + \frac{f(f+1)}{2}\epsilon_{ji}^+$ This term is then added as an additional factor in the maximum likelihood formula.

The postfit histograms are shown in Figure 7.1.

7.1.1.2 Maximum Likelihood Limits

After computing the expected LFV signal branching ratios, the next step is to determine the statistical significance of the result. The profile likelihood $\lambda(\mu)$ is defined as $\lambda(\mu) = \frac{L(\mu, \hat{\theta})}{L(\hat{\mu}, \hat{\theta})}$ where μ is the hypothesized signal strength defined by $\mu = 0$ as the background hypothesis and $\mu = 1$ the signal hypothesis. [19] The nuisance parameters are represented by θ . The denominator is the maximum value of the likelihood function, where $\hat{\mu}$ and $\hat{\theta}$ take their values that maximize the likelihood. The numerator is a likelihood as a function of μ , where $\hat{\theta}$ maximizes the likelihood for a given μ . The profile likelihood can range between 0 and 1. We define our test statistic as $t_\mu = -2\ln\lambda(\mu)$. The probability distribution of this test statistic is given by $t_\mu = \frac{\mu - \hat{\mu}}{\sigma^2} + \mathcal{O}(\frac{1}{\sqrt{N}})$. [37] Here σ is related to the variance of all the nuisance parameters. We can make the asymptotic approximation that the second term goes to zero as $N \rightarrow \infty$. This is known as the asymptotic approximation.

Note that the test statistic is zero for total agreement between the hypothesis and the data and decreases as the data differs more and more from the hypothesis. The probability to observe a given hypothesis μ is defined by $p_\mu = \int_{\mu_{obs}}^{\infty} -2\ln\lambda(\mu)$. The p-value is defined as $p_{\mu=0}$ and is the probability to exclude the background hypothesis. If $p < \alpha$ then we can consider the background hypothesis to be excluded. In high energy physics we define α as 2.87×10^{-7} . It is customary to express the in terms of standard deviations from the mean, assuming a Gaussian probability distribution function (PDF). For a p-value of 2.87×10^{-7} the significance is 5σ .

It is customary to use 95% confidence intervals when setting limits. If $p_\mu < 5\%$ then the hypothesis where the signal strength is μ can be excluded at 95% confidence. However, if the background is very small or fluctuates downward, it is possible to exclude a signal that the analysis is not sensitive to. This can be avoided by using the CL_s method. [36] The p-value for the CL_s method is defined by dividing the p-value for the signal hypothesis by the probability for excluding the background, which is $(1 - p_{\mu=0})$.

It is useful to compare the observed limit with the expected limit. The expected limit is determined by generating an Asimov dataset [19] which is consistent with the background hypothesis. By definition, the Asimov dataset will produce postfit nuisance parameters that are identical to their

expected values. The expected limit is a useful statistic that measures the exclusion power of an analysis. For example, if the expected limit is significantly greater than the signal hypothesis, then the analysis does not have the statistical power to investigate the signal region.

7.1.2 8 TeV Results

The M_{col} distributions after the fit for signal and background contributions are shown in Fig. 7.1 and the event yields in the mass range $100 < M_{\text{col}} < 150 \text{ GeV}$ are shown in Table 7.3. The different channels and categories are combined to set a 95% CL_s upper limit on the branching fraction of LFV Higgs decay in the $\mu\tau$ channel, $B(H \rightarrow \mu\tau)$.

Table 7.1: Event yields in the signal region, $100 < M_{\text{col}} < 150 \text{ GeV}$ after fitting for signal and background. The expected contributions are normalized to an integrated luminosity of 19.7 fb^{-1} . The LFV Higgs boson signal is the expected yield for $B(H \rightarrow \mu\tau) = 0.84\%$ with the SM Higgs boson cross section.

Sample	$H \rightarrow \mu\tau_h$			$H \rightarrow \mu\tau_e$		
	0-Jet	1-Jet	2-Jets	0-Jet	1-Jet	2-Jets
misidentified leptons	1770 ± 530	377 ± 114	1.8 ± 1.0	42 ± 17	16 ± 7	1.1 ± 0.7
$Z \rightarrow \tau\tau$	187 ± 10	59 ± 4	0.4 ± 0.2	65 ± 3	39 ± 2	1.3 ± 0.2
ZZ, WW	46 ± 8	15 ± 3	0.2 ± 0.2	41 ± 7	22 ± 4	0.7 ± 0.2
$W\gamma$	NA	NA	NA	2 ± 2	2 ± 2	NA
$Z \rightarrow ee$ or $\mu\mu$	110 ± 23	20 ± 7	0.1 ± 0.1	1.6 ± 0.7	1.8 ± 0.8	NA
$t\bar{t}$	2.2 ± 0.6	24 ± 3	0.9 ± 0.5	4.8 ± 0.7	30 ± 3	1.8 ± 0.4
$t\bar{t}$	2.2 ± 1.1	13 ± 3	0.5 ± 0.5	1.9 ± 0.2	6.8 ± 0.8	0.2 ± 0.1
SM H background	7.1 ± 1.3	5.3 ± 0.8	1.6 ± 0.5	1.9 ± 0.3	1.6 ± 0.2	0.6 ± 0.1
sum of backgrounds	2125 ± 530	513 ± 114	5.4 ± 1.4	160 ± 19	118 ± 9	5.6 ± 0.9
LFV Higgs boson signal	66 ± 18	30 ± 8	2.9 ± 1.1	23 ± 6	13 ± 3	1.2 ± 0.3
data	2147	511	10	180	128	6

The observed and the median expected 95% CL_s upper limits on the $B(H \rightarrow \mu\tau)$ for the H mass at 125 GeV are given for each category in Table 7.4. Combining all the channels, an expected upper limit of $B(H \rightarrow \mu\tau) < (0.75 \pm 0.38)\%$ is obtained. The observed upper limit is $B(H \rightarrow \mu\tau) < 1.51\%$ which is above the expected limit due to an excess of the observed number of events above the background prediction. The fit can then be used to estimate the branching fraction if this excess were to be interpreted as a signal. The best fit values for the branching fractions are given in Table 7.4. The limits and best fit branching fractions are also summarized graphically in Fig. 7.4. The combined categories give a best fit of $B(H \rightarrow \mu\tau) = (0.84^{+0.39}_{-0.37})\%$. The combined excess is 2.4 standard deviations which corresponds to a p -value of 0.010 at $M_H = 125 \text{ GeV}$.

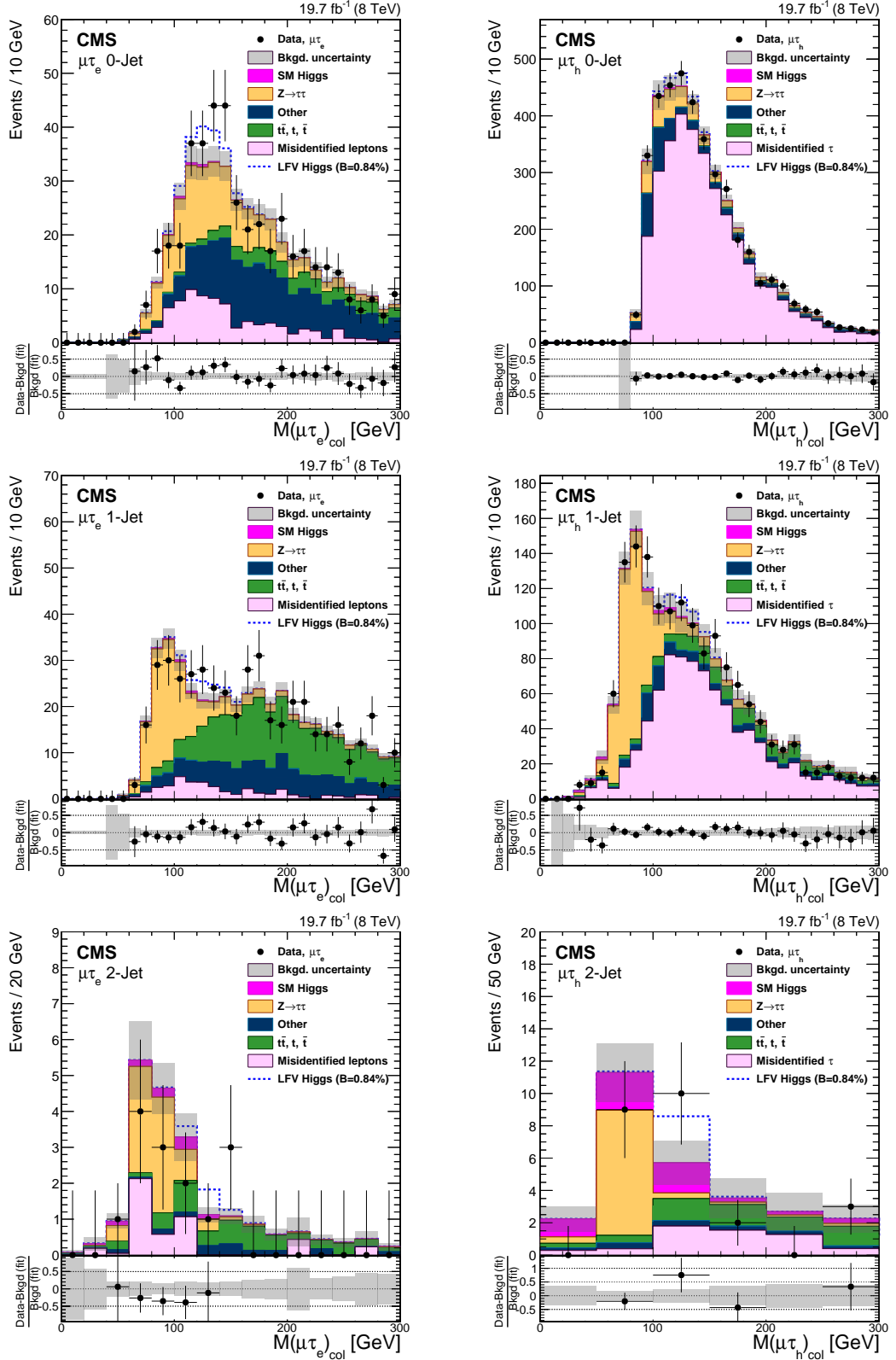


Figure 7.1: Distributions of the collinear mass M_{col} after fitting for signal and background for the LFV $H \rightarrow \mu\tau$ candidates in the different channels and categories compared to data. The distribution of the simulated LFV Higgs boson sample is shown for the best fit branching fraction of $B(H \rightarrow \mu\tau) = 0.84\%$. The bottom panel in each plot shows the fractional difference between the observed data and the fitted background. Top left: $H \rightarrow \mu\tau_e$ 0-jet; top right: $H \rightarrow \mu\tau_h$ 0-jet; middle left: $H \rightarrow \mu\tau_e$ 1-jet; middle right: $H \rightarrow \mu\tau_h$ 1-jet; bottom left: $H \rightarrow \mu\tau_e$ 2-jet; bottom right

Table 7.2: The expected upper limits, observed upper limits and best fit values for the branching fractions for different jet categories for the $H \rightarrow \mu\tau$ process. The one standard-deviation probability intervals around the expected limits are shown in parentheses.

Expected Limits			
	0-Jet (%)	1-Jet (%)	2-Jets (%)
$\mu\tau_e$	$<1.32\ (\pm 0.67)$	$<1.66\ (\pm 0.85)$	$<3.77\ (\pm 1.92)$
$\mu\tau_h$	$<2.34\ (\pm 1.19)$	$<2.07\ (\pm 1.06)$	$<2.31\ (\pm 1.18)$
$\mu\tau$	$<0.75\ (\pm 0.38)$		
Observed Limits			
$\mu\tau_e$	<2.04	<2.38	<3.84
$\mu\tau_h$	<2.61	<2.22	<3.68
$\mu\tau$	<1.51		
Best Fit Branching Fractions			
$\mu\tau_e$	$0.87^{+0.66}_{-0.62}$	$0.81^{+0.85}_{-0.78}$	$0.05^{+1.58}_{-0.97}$
$\mu\tau_h$	$0.41^{+1.20}_{-1.22}$	$0.21^{+1.03}_{-1.09}$	$1.48^{+1.16}_{-0.93}$
$\mu\tau$	$0.84^{+0.39}_{-0.37}$		

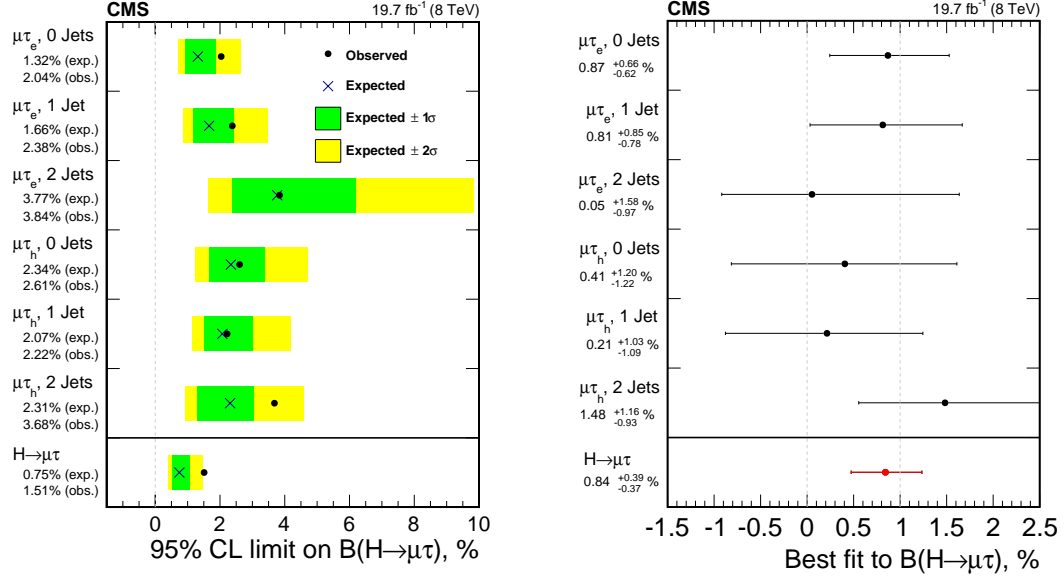


Figure 7.2: Left: 95% CL Upper limits by category for the LFV $H \rightarrow \mu\tau$ decays. Right: best fit branching fractions by category.

7.1.3 13 TeV Results

After applying the full selection cuts, a maximum likelihood fit is performed in the M_{col} variable. Each systematic uncertainty is used as a nuisance parameter in the fit. The distributions of the signal and background contributions after the full selection and the fit are shown in Fig. 7.3 and the event yields in the mass range $100 < M_{\text{col}} < 150 \text{ GeV}$ are shown in Table 7.3. The different channels and categories are combined to set a 95% CL upper limit on the branching fraction of LFV H decay in the $\mu\tau$ channel, $\mathcal{B}(H \rightarrow \mu\tau)$.

Figure 7.3: Distributions of the collinear mass M_{col} after fitting for signal and background for the LFV $H \rightarrow \mu\tau$ candidates in the different channels and categories compared to data. The distribution of the simulated LFV Higgs boson sample is shown for $\mathcal{B}(H \rightarrow \mu\tau) = 10\%$. The bottom panel in each plot shows the fractional difference between the observed data and the fitted background. Top left: $H \rightarrow \mu\tau_e$ 0-jet; top right: $H \rightarrow \mu\tau_h$ 0-jet; middle left: $H \rightarrow \mu\tau_e$ 1-jet; middle right: $H \rightarrow \mu\tau_h$ 1-jet; bottom left: $H \rightarrow \mu\tau_e$ 2-jet; bottom right $H \rightarrow \mu\tau_h$ 2-jet.

Table 7.3: Event yields in the signal region in the range $100 < M_{\text{col}} < 150 \text{ GeV}$. The expected contributions are normalized to an integrated luminosity of 2.3 fb^{-1} . The LFV Higgs boson signal is the expected yield for $\mathcal{B}(H \rightarrow \mu\tau) = 1\%$ with the SM Higgs boson cross section.

Sample	$H \rightarrow \mu\tau_e$			$H \rightarrow \mu\tau_h$		
	0-Jet	1-Jet	2-Jets	0-Jet	1-Jet	2-Jets
misidentified leptons	12.2	5.2	2.8	232.3	54.7	4.7
$Z \rightarrow \tau\tau$	14.4	10.6	1.7	5.3	2.3	0
ZZ, WW	10.7	4.6	3.2	3.2	2.0	0.3
$W\gamma$	1.2	3.4	0.9	NA	NA	NA
$Z \rightarrow ee$ or $\mu\mu$	1.9	2.2	0.3	79.1	11.9	0.1
$t\bar{t}$	1.4	21.8	18.6	1.3	5.4	1.1
t, \bar{t}	0.4	4.1	1.7	0.3	2.2	0.2
SM H background	0.4	0.4	0.4	1.1	0.7	0.3
sum of backgrounds	42.6	52.2	29.6	322.5	79.3	6.6
LFV Higgs boson signal	7.1	3.7	1.9	13.8	4.7	1.2
Observed data	33	41	31	315	77	7

7.1.4 Limit computation

The observed and median expected 95% CL upper limits on the $\mathcal{B}(H \rightarrow \mu\tau)$ for the H mass at 125 GeV are given for each category in Table 7.4. Combining all the channels, an expected upper limit of $\mathcal{B}(H \rightarrow \mu\tau) < (1.62 \pm 0.58)\%$ is obtained. The observed upper limit is $\mathcal{B}(H \rightarrow \mu\tau) < 1.20\%$. The limits are also summarized graphically in Fig. 7.4.

This observed limit on the branching ratio is slightly tighter than the $\mathcal{B}(H \rightarrow \mu\tau) < (1.51 \pm 0.83)\%$ limit obtained using the 19.7 fb^{-1} data sample at 8 TeV analyzed in [?].

Table 7.4: The observed and expected upper limits for different jet categories for the $H \rightarrow \mu\tau$ process. The one standard deviation probability intervals around the expected limits are shown in parentheses.

Expected limits				
	0-jet (%)	1-jet (%)	2-jets (%)	Combined (%)
$\mu\tau_h$	<4.17	<4.89	<6.41	<2.98
$\mu\tau_e$	<2.24	<4.36	<7.31	<1.96
$\mu\tau$	<1.62 %			
Observed limits				
	0-jet (%)	1-jet (%)	2-jets (%)	Combined (%)
$\mu\tau_h$	<4.24	<6.35	<7.71	<3.81
$\mu\tau_e$	<1.33	<3.04	<8.99	<1.15
$\mu\tau$	<1.20 %			
Best fit branching fractions				
	0-jet (%)	1-jet (%)	2-jets (%)	Combined (%)
$\mu\tau_h$	$0.12^{+2.02}_{-1.91}$	$1.70^{+2.41}_{-2.52}$	$1.54^{+3.12}_{-2.71}$	$1.12^{+1.45}_{-1.40}$
$\mu\tau_e$	$-2.11^{+1.30}_{-1.89}$	$-2.18^{+1.99}_{-2.05}$	$2.04^{+2.96}_{-3.31}$	$-1.81^{+1.07}_{-1.32}$
$\mu\tau$	$-0.76^{+0.81}_{-0.84}\%$			

Figure 7.4: 95% CL Upper limits by category for the LFV $H \rightarrow \mu\tau$ decays.

7.2 Limits on lepton flavour violating couplings

Figure 7.5: Constraints on the flavour violating Yukawa couplings, $|Y_{\mu\tau}|$ and $|Y_{\tau\mu}|$. The black dashed lines are contours of $\mathcal{B}(H \rightarrow \mu\tau)$ for reference. The expected limit (red solid line) with one sigma (green) and two sigma (yellow) bands, and observed limit (black solid line) are derived from the limit on $\mathcal{B}(H \rightarrow \mu\tau)$ from the present analysis. The shaded regions are derived constraints from null searches for $\tau \rightarrow 3\mu$ (dark green) and $\tau \rightarrow \mu\gamma$ (lighter green). The light blue region indicates the additional parameter space excluded by our result. The purple diagonal line is the theoretical naturalness limit $Y_{ij}Y_{ji} \leq m_i m_j / v^2$.

The constraint on $\mathcal{B}(H \rightarrow \mu\tau)$ can be interpreted in terms of LFV Yukawa couplings [26]. The LFV decays $H \rightarrow e\mu, e\tau, \mu\tau$ arise at tree level from the assumed flavour violating Yukawa interactions, $Y_{\ell^\alpha \ell^\beta}$ where ℓ^α, ℓ^β denote the leptons, $\ell^\alpha, \ell^\beta = e, \mu, \tau$ and $\ell^\alpha \neq \ell^\beta$. The decay width

$\Gamma(H \rightarrow \ell^\alpha \ell^\beta)$ in terms of the Yukawa couplings is given by:

$$\Gamma(H \rightarrow \ell^\alpha \ell^\beta) = \frac{m_H}{8\pi} (|Y_{\ell^\beta \ell^\alpha}|^2 + |Y_{\ell^\alpha \ell^\beta}|^2),$$

and the branching fraction by:

$$B(H \rightarrow \ell^\alpha \ell^\beta) = \frac{\Gamma(H \rightarrow \ell^\alpha \ell^\beta)}{\Gamma(H \rightarrow \ell^\alpha \ell^\beta) + \Gamma_{SM}}.$$

The SM H decay width is assumed to be $\Gamma_{SM} = 4.1\text{MeV}$ [?] for $M_H = 125\text{GeV}$. The 95% CL constraint on the Yukawa couplings derived from $\mathcal{B}(H \rightarrow \mu\tau) < 1.20\%$ and the expression for the branching fraction above is:

$$\sqrt{|Y_{\mu\tau}|^2 + |Y_{\tau\mu}|^2} < 3.16 \times 10^{-3}.$$

Figure 7.5 compares this result to the constraints from previous indirect measurements.

7.3 W+Jets

7.3.1 Detector Unfolding

The CMS detector, like any experimental instrument, is not infallible. The detector response can cause a measurement to deviate from its true value. For example, for a given event with a leading jet p_T in the 40-45 GeV bin, there is a probability that the jet could have had a p_T in the 35-40 GeV bin or in the 45-50 GeV bin. The detector response can cause the measured value to deviate from its true value. A response matrix is used to transform the measured values to the true values.

A Bayesian unfolding method [?] is used for W+Jets. The i^{th} generated event Gen_i results in a measured event $Reco_i$. The probability of a generated event to be observed in the i^{th} bin is $P(Gen_i)$. The probability that a reco event in bin j is due to a generated event in bin i is $P(Reco_j|Gen_i)$. From those relations, Bayes' theorem [11] is used to obtain $P(Gen_i|Reco_j) =$

$$\frac{P(Reco_j|Gen_i)P(Gen_i)}{\sum_{l=1}^{n_{bins}} P(Reco_j|Gen_l)P(Gen_l)}$$

The probability to observe a reconstructed event in bin j given an generator level even in bin i is given by $P(Reco_j|Gen_i)$. This probability is represented by a matrix, defined as the response matrix (R_{ji}) . The response matrix is calculated by using Monte Carlo (Section 4) to compare generator level events to events reconstructed with detector simulation. It can be visualized for a particular variable by plotting the number of generator level events versus the number of reco

level events. After calculating the response matrix, Bayes' theorem is used to obtain the probability that a reconstructed event in bin j was due to a generator level event in bin i . This probability distribution, $P(Gen_i|Reco_j)$, is referred to as the smearing matrix, S_{ij} .

The number of true events observed in bin i is defined as $\hat{n}(i) = \frac{1}{\epsilon_i} \sum_{j=1}^{n_{bins}} n_{obs}(j) S_{ij}$, where ϵ_i is the efficiency of observing an event that was generated in bin i and is defined by $\epsilon_i = \sum_{j=1}^{n_{bins}} R_{ji}$.

Given the above formulas, the number of true events in each bin can be calculated. The only unknown quantity is $P(Gen_i)$, the probability to observe a generator level event in bin i . This probability is determined by an iterative χ^2 fit. First, $P(Gen_i)$ is estimated from the Monte Carlo distribution. This allows a simple estimation of the true number of events: $\hat{n}_0 = P(Gen_i) N_{obs}$, where N_{obs} is the total number of observed events. Then use Bayes' Theorem to calculate $\hat{n}(i)$ and $\hat{P}(Gen_i)$. The third step is to calculate the χ^2 distribution between $\hat{n}(i)$ and $\hat{n}_0(i)$. The iterative procedure is then repeated, with $\hat{n}(i)$ and $\hat{P}(Gen_i)$ used in the first step. The iterative procedure is repeated at least four times and is concluded when $\chi^2/\nu < \frac{1}{\sqrt{2}}$.

7.3.2 13 TeV Results

Chapter 8

Conclusions

8.1 Summary

8.2 Future Outlook

Bibliography

- [1] Wolfgang Adam, R Frhwirth, Are Strandlie, and T Todor. Reconstruction of Electrons with the Gaussian-Sum Filter in the CMS Tracker at the LHC. Technical Report CMS-NOTE-2005-001, CERN, Geneva, Jan 2005.
- [2] Q. R. Ahmad et al. Measurement of the rate of $\nu_e + d \rightarrow p + p + e^-$ interactions produced by 8B solar neutrinos at the Sudbury Neutrino Observatory. *Phys. Rev. Lett.*, 87:071301, 2001.
- [3] Q. R. Ahmad et al. Direct evidence for neutrino flavor transformation from neutral current interactions in the Sudbury Neutrino Observatory. *Phys. Rev. Lett.*, 89:011301, 2002.
- [4] Simone Alioli, Paolo Nason, Carlo Oleari, and Emanuele Re. A general framework for implementing NLO calculations in shower Monte Carlo programs: the POWHEG BOX. *JHEP*, 06:043, 2010.
- [5] John Allison et al. Geant4 developments and applications. *IEEE Trans. Nucl. Sci.*, 53:270, 2006.
- [6] J. Alwall, R. Frederix, S. Frixione, V. Hirschi, F. Maltoni, O. Mattelaer, H. S. Shao, T. Stelzer, P. Torrielli, and M. Zaro. The automated computation of tree-level and next-to-leading order differential cross sections, and their matching to parton shower simulations. *JHEP*, 07:079, 2014.
- [7] J R Andersen et al. Handbook of LHC Higgs Cross Sections: 3. Higgs Properties. 2013.
- [8] Nima Arkani-Hamed, Savas Dimopoulos, and G. R. Dvali. The Hierarchy problem and new dimensions at a millimeter. *Phys. Lett.*, B429:263–272, 1998.
- [9] Vernon D. Barger and Roger J. N. Phillips. *Collider Physics (Frontiers in Physics)*. Addison Wesley Publishing Company, 1987.
- [10] G. W. Bennett et al. Measurement of the negative muon anomalous magnetic moment to 0.7 ppm. *Phys. Rev. Lett.*, 92:161802, 2004.
- [11] Philip Bevington and D. Keith Robinson. *Data Reduction and Error Analysis for the Physical Sciences*. McGraw-Hill Education, 3rd edition, 7 2002.
- [12] G. C. Branco, P. M. Ferreira, L. Lavoura, M. N. Rebelo, Marc Sher, and Joao P. Silva. Theory and phenomenology of two-Higgs-doublet models. *Phys. Rept.*, 516:1–102, 2012.

- [13] Matteo Cacciari, Gavin P. Salam, and Gregory Soyez. The Anti-k(t) jet clustering algorithm. *JHEP*, 04:063, 2008.
- [14] Serguei Chatrchyan et al. Observation of a new boson at a mass of 125 GeV with the CMS experiment at the LHC. *Phys. Lett.*, B716:30–61, 2012.
- [15] Serguei Chatrchyan et al. The performance of the CMS muon detector in proton-proton collisions at $\sqrt{s} = 7$ TeV at the LHC. *JINST*, 8:P11002, 2013.
- [16] Serguei Chatrchyan et al. Description and performance of track and primary-vertex reconstruction with the CMS tracker. *JINST*, 9(10):P10009, 2014.
- [17] CMS Collaboration. Performance of ℓ -lepton reconstruction and identification in cms. *Journal of Instrumentation*, 7(01):P01001, 2012.
- [18] J. S. Conway. Incorporating Nuisance Parameters in Likelihoods for Multisource Spectra. In *Proceedings, PHYSTAT 2011 Workshop on Statistical Issues Related to Discovery Claims in Search Experiments and Unfolding, CERN, Geneva, Switzerland 17-20 January 2011*, 2011.
- [19] Glen Cowan, Kyle Cranmer, Eilam Gross, and Ofer Vitells. Asymptotic formulae for likelihood-based tests of new physics. *Eur. Phys. J.*, C71:1554, 2011. [Erratum: *Eur. Phys. J.* C73,2501(2013)].
- [20] S. Dittmaier et al. Handbook of LHC Higgs Cross Sections: 1. Inclusive Observables. 2011.
- [21] Stefano Frixione, Paolo Nason, and Carlo Oleari. Matching NLO QCD computations with Parton Shower simulations: the POWHEG method. *JHEP*, 11:070, 2007.
- [22] R. Fruhwirth. Application of Kalman filtering to track and vertex fitting. *Nucl. Instrum. Meth.*, A262:444–450, 1987.
- [23] Y. Fukuda et al. Evidence for oscillation of atmospheric neutrinos. *Phys. Rev. Lett.*, 81:1562–1567, 1998.
- [24] D.J. Griffiths. *Introduction to Electrodynamics*. Prentice Hall, 1999.
- [25] F. Halzen and Alan D. Martin. Quarks and leptons: An introductory course in modern particle physics. 1984. New York, Usa: Wiley (1984) 396p.
- [26] Roni Harnik, Joachim Kopp, and Jure Zupan. Flavor Violating Higgs Decays. *JHEP*, 03:026, 2013.
- [27] Andreas Hocker et al. TMVA - Toolkit for Multivariate Data Analysis. *PoS*, ACAT:040, 2007.
- [28] Vardan Khachatryan et al. Differential cross section measurements for the production of a W boson in association with jets in protonproton collisions at $\sqrt{s} = 7$ TeV. *Phys. Lett.*, B741:12–37, 2015.

- [29] Vardan Khachatryan et al. Performance of Electron Reconstruction and Selection with the CMS Detector in Proton-Proton Collisions at $s = 8$ TeV. *JINST*, 10(06):P06005, 2015.
- [30] Vardan Khachatryan et al. Performance of the CMS missing transverse momentum reconstruction in pp data at $\sqrt{s} = 8$ TeV. *JINST*, 10(02):P02006, 2015.
- [31] Henning Kirschenmann. Jet performance in CMS. Technical Report CMS-CR-2013-325, CERN, Geneva, Oct 2013.
- [32] Paolo Nason. A New method for combining NLO QCD with shower Monte Carlo algorithms. *JHEP*, 11:040, 2004.
- [33] K. A. Olive et al. Review of Particle Physics. *Chin. Phys.*, C38:090001, 2014.
- [34] J. Pumplin, D. R. Stump, J. Huston, H. L. Lai, Pavel M. Nadolsky, and W. K. Tung. New generation of parton distributions with uncertainties from global QCD analysis. *JHEP*, 07:012, 2002.
- [35] Lisa Randall and Raman Sundrum. A Large mass hierarchy from a small extra dimension. *Phys. Rev. Lett.*, 83:3370–3373, 1999.
- [36] A L Read. Modified frequentist analysis of search results (the CL_s method). (CERN-OPEN-2000-205), 2000.
- [37] A. Wald. *Tests of Statistical Hypotheses Concerning Several Parameters when the Number of Observations is Large*. American Mathematical Society, 1943.
- [38] Zbigniew Was. TAUOLA for simulation of tau decay and production: perspectives for precision low energy and LHC applications. *Nucl. Phys. Proc. Suppl.*, 218:249–255, 2011.